FACULTY OF TECHNICAL PHYSICS
POZNAN UNIVERSITY OF TECHNOLOGY

PREPARATION AND MAGNETIC PROPERTIES OF MAGNONIC THIN FILM STRUCTURES

Filip LISIECKI

Thesis supervisor:
Prof. Dr Feliks STOBIECKI
Supervisors:
Dr Eng. Piotr KUŚWIK
M.Sc. Eng. Michał MATCZAK

Poznań, 2015

Acknowledgments

I would like to thank Prof. Dr Feliks Stobiecki for supervision of my thesis, discussions and great support. I am also very grateful to Dr Eng. Piotr Kuświk for giving me insight in lithography and different measurement techniques, his great mentoring and all time he spent explaining me different issues related to my thesis but not only. I also want to thank Prof. Dr Andrzej Maziewski for giving me the opportunity to participate in the SYMPHONY project and enabling measurements at the University of Białystok.

I would like to express my gratitude to all other people who contributed to this work. In particular:

- M.Sc. Eng. Michał Matczak for insight in lithography techniques and supervision,
- M.Sc. Eng. Hubert Głowiński for insight into the FMR techniques, help with measurements and fruitful discussions about the results,
- collaborators from Prof. Maziewski's group from the University of Białystok, in particular Dr Zbigniew Kurant and M.Sc. Nadeem Tahir for help with MOKE measurements and Dr Piotr Mazalski for providing MFM images,
- collaborators from Prof. Dr Maciej Krawczyk's group from the Adam Mickiewicz University for providing micromagnetic simulations and help in understanding the spin excitation results,
- B.Sc. Eng. Łukasz Frąckowiak for collaborative efforts.

The research has received funding from the project SYMPHONY (program TEAM/2011-8/4) of the Foundation for Polish Science.

Abstract

The main goal of this thesis was to fabricate one-dimensional magnonic crystals from $Ni_{80}Fe_{20}$ stripes using electron-beam lithography and lift-off technique, and measure their static and dynamic magnetic properties. The stripes form periodic and, by obeying the Fibonacci rule, quasiperiodic structures. To measure their dynamic magnetic properties, the structures were integrated with coplanar waveguides and fabricated using direct laser writing. For both fabrication techniques, optimization was performed.

Static magnetic properties were studied with magneto optical Kerr effect and magnetic force microscope. These methods allowed measurements of the hysteresis loops and imaging the magnetization switching in the stripes. Magnetization dynamics was studied using ferromagnetic resonance with vector network analyzer. In the periodic structures one coercive field was found associated with the spectra typical of an array of periodic stripes. However, for quasiperiodic arrays two coercivity fields, related to switching of magnetization direction in the stripes of different width and additional excitation modes were observed..

Streszczenie

Celem tej pracy magisterskiej było wykonanie, przy użyciu litografii elektronowej i techniki lift-off, jednowymiarowych kryształów magnonicznych złożonych z pasków $Ni_{80}Fe_{20}$ i zbadanie ich statycznych i dynamicznych właściwości magnetycznych. Paski te tworzą struktury periodyczne oraz, spełniające regułę Fibonacciego, kwazi-periodyczne. Aby zmierzyć dynamiczne właściwości magnetyczne, struktury zostały zintegrowane z falowodami koplanarnymi, wytworzonymi przy pomocy fotolitografii bezmaskowej. Dla obu technik preparacji została przeprowadzona optymalizacja.

Statyczne właściwości magnetyczne były badane przy pomocy magneto optycznego efektu Kerra oraz mikroskopu sił magnetycznych. Pozwoliło to na zmierzenie pętel histerezy oraz zobrazowanie przełączania magnetyzacji w paskach. Dynamika namagnesowania była badana przy pomocy rezonansu ferromagnetycznego z wektorowym analizatorem sieci. W strukturach periodycznych zaobserwowano jedno pole koercji zgodnie z tym, co rejestruje się dla struktur periodycznych. Jednakże dla kwazi-periodycznych struktur zaobserwowano dwa pole koercji, związane z przełączaniem magnetyzacji w paskach o różnej szerokości, a także dodatkowe mody.

CONTENT

INTRODUCTION

In recent years a lot of interest have been paid to spin waves dynamics in periodic nanopatterned magnetic materials. One of the main reason for this interest is that it is possible to modify their spin waves excitation spectra by their topology, which can be determined by the patterning process. What is more, their magnonic band structure consists of allowed and forbidden frequency band gaps of magnons propagation. These properties can be tailored not only by the sample geometry, but they also depend strongly on the magnetic properties (magnetization, exchange constant, Gilbert damping) of used material [2]. This also means they are easily tunable by external magnetic field [3].

Magnetic stripes array is one of the several geometries which have already been investigated. They could have potential application in microwave devices [4], domain wall logic [5], transmission, processing and storage of information [6]. They realize one-dimensional magnonic crystals and are a great model to study the excitation of spin waves in confined magnetic systems [7] and disorder on periodical lattices [8]. In this thesis the arrays of periodic and quasiperiodic $Ni_{80}Fe_{20}$ stripes are studied. The periodic $Ni_{80}Fe_{20}$ stripes arrays have been already investigated for example in [8], [9] and this type of structure is assumed as a reference. The main interest of this thesis is in the quasiperiodic structure, which is prepared by obeying the Fibonacci rule. According to the best of our knowledge, stuctures of this type have not been experimentally investigated yet.

1. THEORY

In this chapter a theory of ferromagnetism is briefly described, including classification of materials according to their magnetic properties, description of different energy contributions and magnetization dynamics. Moreover, the conception of spin waves is introduced along with that of periodically modulated magnetic materials – magnonic crystals.

1.1. Ferromagnetism

1.1.1. Basics

Magnetic moment in atoms is related to the inner angular momentum of electrons – spin, orbital angular momentum of electrons caused by their circulation around core and external magnetic field influencing the orbital angular momentum. The first two bring the paramagnetic contribution to magnetization and the last one brings the diamagnetic one. There is also angular momentum of atomic core, although its value is so small that can be neglected. Magnetic materials can be classified according to the tensor of magnetic susceptibility $\hat{\chi}$ which depends on the response of magnetization **M** to an external magnetic field **H** described by the relation:

$$\boldsymbol{M} = \hat{\chi}\boldsymbol{H} \tag{1.1}$$

where **M** is a sum of magnetic moments per volume of a medium:

$$\boldsymbol{M} = \frac{d\boldsymbol{m}}{V}. \tag{1.2}$$

We can also define the magnetic flux **B** as:

$$\boldsymbol{B} = \mu_0(\boldsymbol{M} + \boldsymbol{H}) = \mu_0(\chi + 1)\boldsymbol{H} \tag{1.3}$$

where μ_0 is the permeability of vacuum ($\mu_0 = 4\pi \cdot 10^{-7}\,\frac{Vs}{Am}$). For diamagnetic materials the value of χ simplified to a scalar is < 0 which means that **M** is antiparallel to the external field. In these materials all spins are compensated and thus the spin and orbital magnetic momentum is equal zero. Paramagnetic materials ($\chi > 0$) have at least one uncompensated electron contributing to the magnetic moment. In an external magnetic field, magnetic moments of atoms tend to align with field lines. Ferromagnetic and ferrimagnetic materials have the susceptibility $\chi \gg 0$. They exhibit spontaneous magnetization, which means that below a critical temperature (the Curie temperature) they can retain a finite magnetization even without external field **H**. The difference between these two is that we can consider ferrimagnetics as consisting of at least two

ferromagnetic sublattices with the opposite magnetic moments, which bring uneven contributions to the spontaneous magnetization.

1.1.2. Energy contribution

In ferromagnetic materials, the orientation of magnetic moments is determined by the minimum of the total energy of the system. Different interactions contribute to this total energy through different energy terms and define the magnetic domain structure in ferromagnetic materials. A domain is a region in which all microscopic magnetic moments **m** are arranged in parallel to each other. The relevant energy terms are:

- exchange energy
- Zeeman energy
- demagnetization energy
- anisotropy energy.

The quantum exchange interaction enforces the arrangement of spins in the same direction. It is based on the Coulomb interaction and the Pauli Exclusion Principle. Its energy can be described as:

$$E_{ex} = -2J_{ij}(\boldsymbol{S_i} \cdot \boldsymbol{S_j}) \qquad 1.4$$

where $\boldsymbol{S_i}$ and $\boldsymbol{S_j}$ represent the electron spin operators of atoms *i* and *j* respectively, whereas J_{ij} is the exchange integral which characterizes the strength of this interaction. Although quantum exchange interaction falls off very rapidly and can be considered nearly as a next-neighbor interaction, because its strength it is responsible for long range ordering in ferromagnetics [10].

The next energy term is the Zeeman energy E_z, which describes the interaction between the magnetization **M** and the external magnetic field **H**. A ferromagnetic material placed in magnetic field is subjected to the torque $\boldsymbol{HxM}$ tending to align magnetic moments parallel to the field lines. This energy term is described as:

$$E_Z = -\mu_0 \int dV \boldsymbol{M} \cdot \boldsymbol{H}. \qquad 1.5$$

The Zeeman energy is minimalized when the magnetization is aligned in parallel to the external field.

Demagnetization energy is connected to the long-reaching dipole-dipole interaction between magnetic moments which, in contrast to the exchange interaction, favors antiparallel arrangement. This energy term is:

$$E_{dem} = -\frac{1}{2}\int dV \boldsymbol{M} \cdot \boldsymbol{H_{dem}} \qquad 1.6$$

The factor ½ appears so that the interaction of each dipole with magnetic field is taken only once. The formation of magnetic domains is driven by minimization of this energy. $\mathbf{H_{dem}}$ is the demagnetization field which in general is a complex spatial function. This energy is therefore related to the magnetic field, which is generated by the magnetic material itself. We can write, that:

$$\boldsymbol{H_{dem}} = \widehat{N}\boldsymbol{M} \qquad 1.7$$

where $\widehat{N}$ is demagnetization tensor dependent on the geometrical shape of the sample.

The last described here energy contribution is anisotropy energy. Its value depends on the magnetization orientation with respect to some axes. The directions for which this energy is minimal and maximal are called the easy and hard axis, respectively. There are different types of anisotropy. The most common is magnetocrystalline, caused by the spin-orbit interaction. Spin moment interacts with orbital moment which is bounded to the crystal structure. Because of that in some directions defined by the crystal lattice it is easier to magnetize the ferromagnetic crystal. Another type of anisotropy is the shape anisotropy, which is important for thin films. It depends on the geometrical shape of the sample and it is caused by the formation of demagnetization field inside material. For example, for materials with spheroidal shape the anisotropy coefficient K_{sh} can be described as:

$$K_{sh} = \frac{1}{2}\mu_0(N_1 - N_3)M^2 \qquad 1.8$$

where N_1 and N_3 are demagnetization factors for different **M** orientation with respect to the main axes of the spheroid [11]. For the sphere $N_1 = N_3$ and as a result the shape anisotropy is equal zero. Magnetic anisotropy can be also induced by tension which can distort the crystal lattice and therefore change the spin-orbit interaction. This phenomenon is called the reverse magnetostriction effect. When tension is applied along a specific direction it is uniaxial anisotropy, with the easy axis related to this direction. Another method of inducing the uniaxial anisotropy in ferromagnetic alloys (e.g. in permalloy = $Ni_{80}Fe_{20}$) is to apply magnetic field during layer deposition

or on heating the sample. After this process or after cooling the sample down to the room temperature, the anisotropy with the easy axis aligned with the earlier applied field is induced. It happens because the magnetic field causes some arrangement in the material, which is frozen on the cooling. In thin layers anisotropy can be also modified by tension caused by differences in the lattice constants of the substrate and the deposited film or by differences in the thermal expansion coefficients. Furthermore, when in some material there are different kinds of anisotropy, usually one of them dominates over the others and therefore determines the local direction of the magnetic moments without an external magnetic field applied.

While decreasing a thickness of ferromagnetic film, the ratio of its surface area to volume is rising. It is significant because surface atoms have reduced symmetry in comparison to the volume atoms. Spins on the surface have "neighbors" only on one side thus their exchange energy differs than that in the bulk of the sample. The energy related to the surface anisotropy drives the magnetic moments to assume positions parallel or perpendicular to the surface. With decreasing thickness of ferromagnetic layer this type of anisotropy can dominate over the other ones and can be used to arrange the easy axis in a selected direction [12]. An example is shown in Figure 1.1 showing the dependence of effective anisotropy coefficient K_{eff} multiplied by layer thickness t_F on this thickness. We can write this relationship as:

$$K_{eff} \cdot t_F = K_V \cdot t_F + 2K_S \qquad 1.9$$

where K_V and K_S are coefficients of volume and surface anisotropy respectively. For thick layers the volume anisotropy dominates, therefore the easy axis lies in-plane of the sample ($K_{eff} < 0$). With the thickness t_F decreasing below some value, the surface anisotropy starts to dominate changing the easy axis direction to be perpendicular to the sample surface ($K_{eff} > 0$).

The total energy *E* of the system is sum of all energy contributions listed above. By finding its minimum we can determine the equilibrium configuration of magnetization. The competition between different terms can cause magnetic moments to point locally in different directions and cause complex domain formation. By using this total energy we can introduce the effective magnetic field which acts on the magnetic material:

$$\boldsymbol{H_{eff}} = -\frac{\partial E}{\partial \boldsymbol{M}}. \qquad 1.10$$

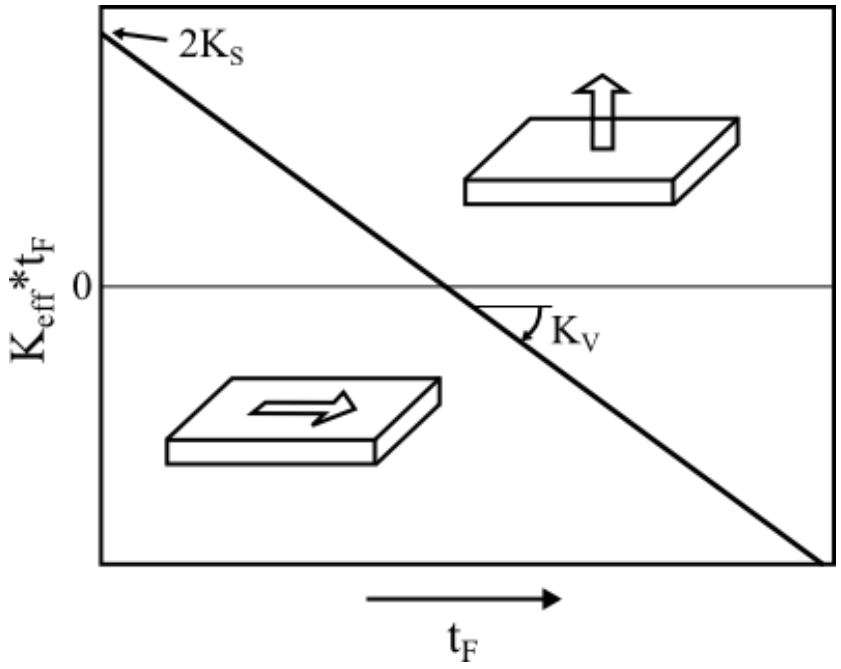

Figure 1.1 Dependence of the effective anisotropy coefficient multiplied by the ferromagnetic layer thickness versus this thickness. This dependence is described by Eq. 1.9.

1.1.3. Magnetization dynamics

In the previous chapter we described relevant contributions to static magnetic behavior and now we turn to magnetization dynamics. We consider a macrospin model in which **M** is a single macro spin representing a sum of all magnetic moments in the sample. For simplicity we can assume that the Zeeman energy is dominant, which means that external field **H** applied is high enough to saturate the ferromagnetic material. According to the dynamical model proposed by Landau and Lifshitz in 1935 [13]:

$$\frac{d\boldsymbol{M}}{dt} = -\gamma\mu_0 \boldsymbol{M}x\boldsymbol{H_{eff}} \qquad 1.11$$

where γ is the gyromagnetic ratio. Misalignment of the magnetization from the effective magnetic field direction creates a torque which causes a continuous precession of the magnetization (see Figure 1.2a).

The behavior of magnetization **M** described by Eq. 1.11 (an infinitely long precession around the equilibrium state) is not observed in experiments. To describe a factual case, one needs to include into the Landau-Lifshitz equation a phenomenological damping term:

$$\frac{d\boldsymbol{M}}{dt} = -\gamma\mu_0 \boldsymbol{M}x\boldsymbol{H_{eff}} - \frac{\lambda}{M_{sat}} \boldsymbol{M}x(\boldsymbol{M}x\boldsymbol{H_{eff}}) \qquad 1.12$$

where M_{sat} is an absolute value of the saturation magnetization and λ is a damping parameter. In the real situation, besides the precession of the macrospin we have also a force component which points toward the center of the circular motion. As a result, after a finite time, **M** aligns with $\mathbf{H_{eff}}$ (see Figure 1.2b). Unfortunately, the damping term in Landau-Lifshitz equation fails for large λ values. That is why Gilbert proposed a different form of the damping term to be used in the Landau-Lifshitz-Gilbert equation [14]:

$$\frac{d\boldsymbol{M}}{dt} = -\gamma\mu_0\, \boldsymbol{M}x\boldsymbol{H_{eff}} - \frac{\alpha}{M_{sat}}\left(\boldsymbol{M}x\frac{d\boldsymbol{M}}{dt}\right) \qquad 1.13$$

with α as the damping parameter. For small values of α, equations 1.12 and 1.13 are equivalent.

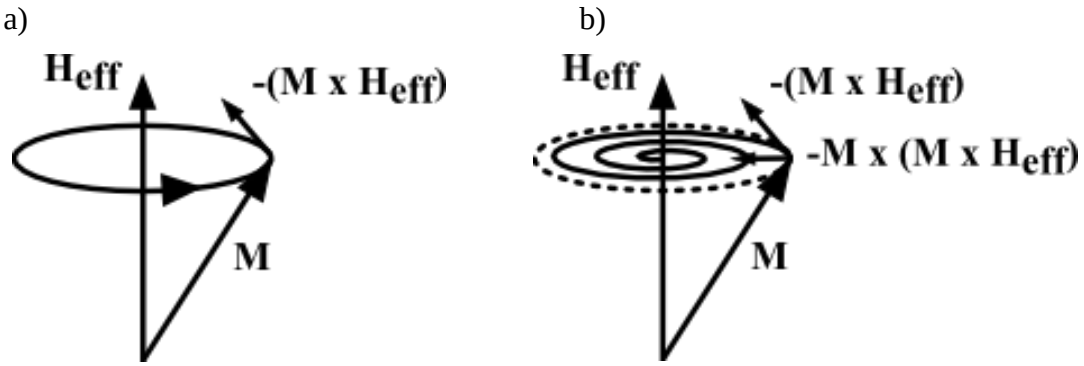

*Figure 1.2 Precession of the macrospin magnetization **M** around the effective field $\mathbf{H_{eff}}$ without (a) and with (b) damping. **M** x $\mathbf{H_{eff}}$ is perpendicular to the field and the magnetization. For motion damping, the radius of precession is decreasing until **M** and $\mathbf{H_{eff}}$ are parallel.*

Finding an analytical solution for the Landau-Lifshitz-Gilbert equation is in general not possible. Although under several assumptions this equation can be solved for a thin ferromagnetic film, what is important in relation to this thesis. We assume that the thin film lies in the *xy*-plane and thanks to that the demagnetization factors are $N_x = N_y = 0$ and $N_z = 1$. Moreover, we consider a uniaxial anisotropy with the easy axis lying along the *x*-direction. This means magnetization is parallel to the effective field and the *x*-axis. Furthermore, the excitation field is perpendicular to the effective field and points along the *y*-direction. Another assumption is the uniform excitation i.e. a wave vector *k=0*. The perpendicular anisotropy of the surface is also considered but with values small enough not to exceed the demagnetization field. After ref. [15], [16] we can give the equations for the real and imaginary party of the susceptibility:

$$\Re(\chi_{yy}) = \chi'_{yy} = \frac{\omega_M(\omega_H + \omega_{eff})(\omega_{res}^2 - \omega^2)}{(\omega_{res}^2 - \omega^2)^2 + \alpha^2\omega^2(2\omega_H + \omega_{eff})^2}, \quad 1.14$$

$$\Im(\chi_{yy}) = \chi''_{yy} = \frac{\alpha\omega\omega_M\left[\omega^2 + (\omega_H + \omega_{eff})^2\right]}{(\omega_{res}^2 - \omega^2)^2 + \alpha^2\omega^2(2\omega_H + \omega_{eff})^2} \quad 1.15$$

with following terms:

$$\omega_M = \gamma\mu_0 M_s;\ \omega_H = \gamma\mu_0(H_{ext} + H_{uni});\ \omega_{eff} = \gamma\mu_0 M_{eff}, \quad 1.16$$

where $H_{uni} = \frac{2K_u}{\mu_0 M_{sat}}$ includes the uniaxial anisotropy and M_{eff} contains the contribution of the surface anisotropy:

$$M_{eff} = M_{sat} - \frac{2K_S}{t_F\mu_0 M_{sat}}. \quad 1.17$$

In Figure 1.3 the real and imaginary parts of the susceptibility are presented. A Lorentzian function can be used to approximate the imaginary part curve. Its full width half maximum (FWHM) – the frequency linewidth $\Delta\omega$, is connected with the damping parameter α by the approximation:

$$\Delta\omega = \alpha(2\omega_H + \omega_{eff}). \quad 1.18$$

The dependence of the real part has two extremes, and the difference in their frequencies is equal to the FWHM of the imaginary part. Moreover, the frequency at which the Lorentzian function has its maximum is called the resonance frequency:

$$\omega_{res}^2 = \omega_H(\omega_{eff} + \omega_H). \quad 1.19$$

This equation is a special case of the Kittel formula [17], which in general, considering the demagnetization factors states that:

$$f_{res} = \frac{\gamma\mu_0}{2\pi}\sqrt{(H_{ext} + (N_y - N_x)M_{sat})(H_{ext} + (N_z - N_x)M_{sat})}. \quad 1.20$$

It is valid for the ferromagnetics with homogenous internal field. Using this equation, it is possible to determine M_{sat} from the field-dependent ferromagnetic resonance (FMR) measurements [15].

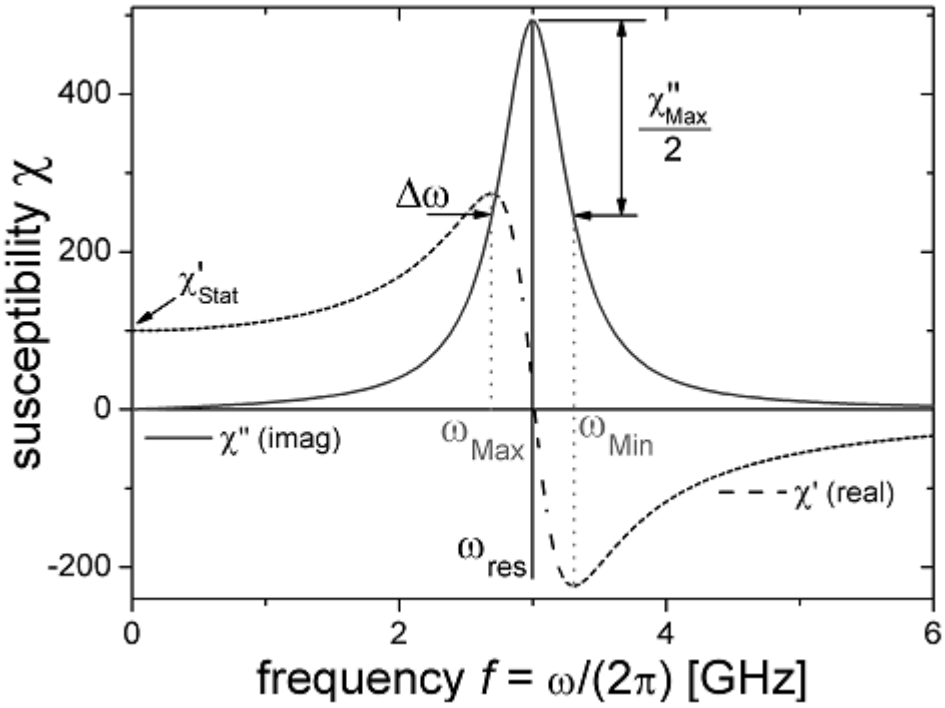

Figure 1.3 The real (dashed line) and imaginary (straight line) of the complex susceptibility χ_{yy} for the parameters: $\gamma/(2\pi) = 30GHz/T, \mu_0 M_{sat} = 1T \approx \mu_0 M_{eff}, \mu_0 H_{ext} = 0.01T, \alpha = 0.02$ [18].

1.2. Spin waves

The previous discussions were related to the uniform magnetization precession i.e. to the situation when all spins had the same precession frequency and phase and therefore the wave vector $\boldsymbol{k} = 0$ which implies infinite wavelength. Now let us consider excitations with a finite wavelength (non-zero wave vector) which are called spin waves (SWs) whose quanta are called magnons (see Figure 1.4). We can distinguish two types of interactions related to the propagation of spin waves. The first is the exchange interaction, which dominates in spin waves of short wavelengths, and the second is the dipole interaction, dominating in long-wavelength spin waves, called also magnetostatic waves. The fundamental equation, which describes the magnetostatic modes in homogenous media, is called the Walker's equation [19]:

$$(1+\chi)\left[\frac{\partial^2\Psi}{\partial x^2}+\frac{\partial^2\Psi}{\partial y^2}\right]+\frac{\partial^2\Psi}{\partial z^2}=0 \qquad 1.21$$

where Ψ is the magnetostatic scalar potential, thus $\boldsymbol{H} = -\nabla\Psi$.

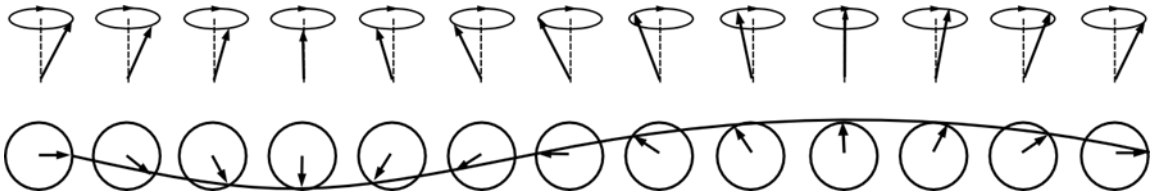

Figure 1.4 The spin wave propagating in the spin chain. Top: view from one side; bottom: view from the top. The line at the bottom connects the ends of spin vectors; after [10].

Assuming that $\Psi \propto \exp(i\boldsymbol{k}\cdot\boldsymbol{r})$, which means that the scalar potential is proportional to the propagation rate of a uniform plane wave, we can find the dispersion relation:

$$(1+\chi)\left(k_x^2+k_y^2\right)+k_z^2=0. \qquad 1.22$$

In thin ferromagnetic films, which are investigated in this thesis, the out-of-plane term k_z of the wave vector is quantized because of the finite thickness of the film:

$$k_z = n\frac{\pi}{t_F}, n \in \mathbb{N}. \qquad 1.23$$

By choosing different boundary conditions and direction relations of the in-plane wave vector $k_{||}=\sqrt{k_x^2+k_y^2}$ and magnetization to the film plane, we can obtain different magnetostatic modes. Three of them that can be found in thin films are described in this thesis (see Figure 1.5) [19]. Anisotropy and exchange interaction are here omitted. The first is **magnetostatic surface wave (MSSW)**, also called the Damon-Eshbach mode or surface spin waves. The term "surface" comes from the fact that its amplitude decays exponentially from the surface of the film. This mode occurs when magnetization lies in-plane of the film and $k_{||} \perp \boldsymbol{M}$. The dispersion is given by:

$$\omega_{MSSW}^2=\omega_H\left(\omega_H+\omega_{eff}\right)+\frac{\omega_{eff}^2}{4}\left[1-e^{-2k_{\|}t_F}\right] \qquad 1.24$$

This is a forward mode, because the directions of the phase and group velocities, which are defined respectively as:

$$v_p=\frac{\omega}{k}, \qquad v_g=\frac{\partial\omega}{\partial k} \qquad 1.25$$

are the same. If for the same direction of magnetization (in-plane of the sample) $k_{||} \parallel \boldsymbol{M}$, the **magnetostatic backward volume waves (MSBVM)** propagate. In this mode, the amplitude is sinusoidally distributed throughout the film volume. Moreover, because of the negative slope of the dispersion relation, the group velocity is negative and points to the opposite direction than the phase velocity. That is why it is called a backward wave. The dispersion relation is as follow:

$$\omega_{MSBVM}^2 = \omega_H \left[\omega_H + \omega_{eff} \left(\frac{1 - e^{-k_\parallel t_F}}{k_\parallel t_F} \right) \right] \qquad 1.26$$

The last mode is the **magnetostatic forward volume wave (MSFVW)** which occurs when magnetization is perpendicular to the sample surface and the wave vector lies in plane of the sample. As in MSBVM, the wave amplitude is sinusoidally distributed in the film volume. Furthermore, it is a forward wave because of the same direction of the phase and group velocities. In this mode dispersion relation does not depend on the direction of the $k_{||}$, so the propagation (without considering the magnetic anisotropy) of the wave is isotropic in the film plane. The dispersion relation is:

$$\omega_{MSFVM}^2 = \omega_H \left[\omega_H + \omega_{eff} \left(1 - \frac{1 - e^{-k_\parallel t_F}}{k_\parallel t_F} \right) \right]. \qquad 1.27$$

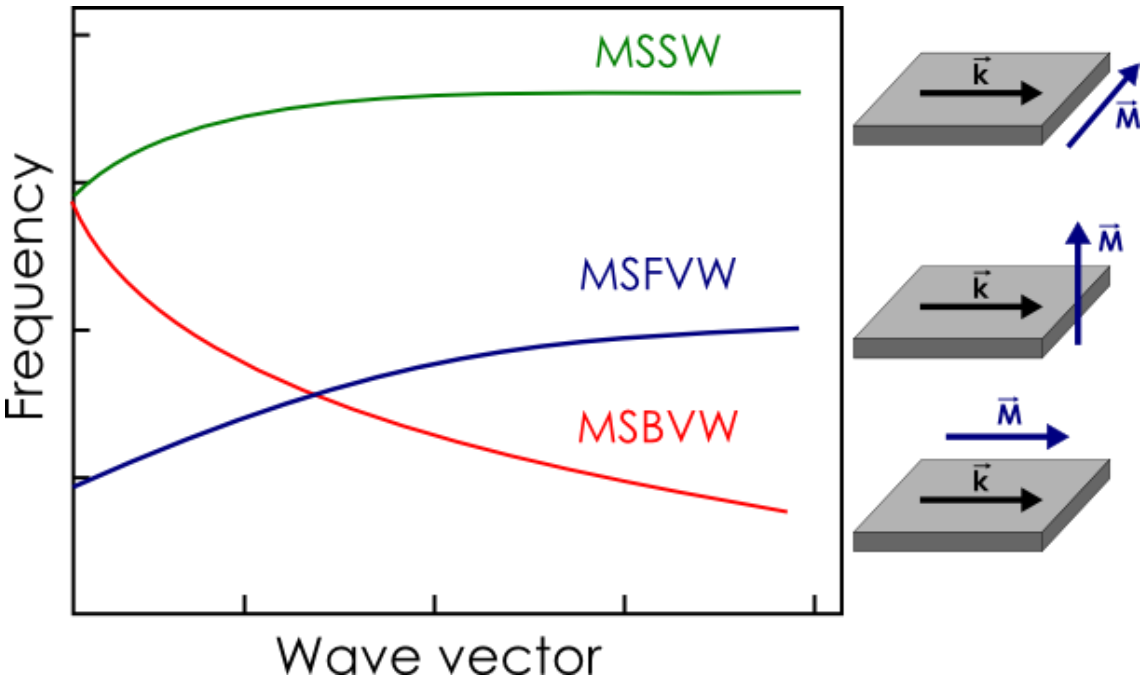

*Figure 1.5 Schematic spin wave dispersion for three magnetostatic modes. On the right: configurations of magnetization **M**, wave vector **k** and sample plane for the corresponding modes. Based on [20]*

1.3. Magnonic crystals

Propagation of different kinds of waves in periodically modulated materials has recently become the subject of interest of many researchers. Magnonic crystals (MCs) which are considered magnetic analogue of photonic crystals also belong to this group. They are magnetic metamaterials showing periodically modulated magnetic properties like saturation magnetization M_{sat} or anisotropy or they can be subjected to modulating parameters (i.e. external magnetic field or stress) which modify the propagation of spin waves in the bulk. We can divide MCs into three types, depending

on the dimensionality of the structure: one- (1D), two- (2D) or three-dimensional (3D) (see Figure 1.6). Because of this periodicity, waves can be coherently scattered and undergo Bragg reflection. It gives rise to formation of partial or complete band gaps, which are the frequency ranges of magnons that cannot propagate in the structure. Additionally, in the case of magnonic crystals, not only periodic pattern, but also spatial distribution of magnetization vectors influences the band structure which can be changed during the magnonic device operation. Magnonic structures should offer new, currently unavailable in photonic and electronic structures functionalities. They can be easily manipulated by the external magnetic field and offer a possibility of further miniaturization, because spin waves wavelength is several orders smaller than that of the electromagnetic wave at the same frequency. Besides that they could offer low energy consumption and possibility of ultrafast operation and reprogrammability at the sub-nanosecond time range [2], [3].

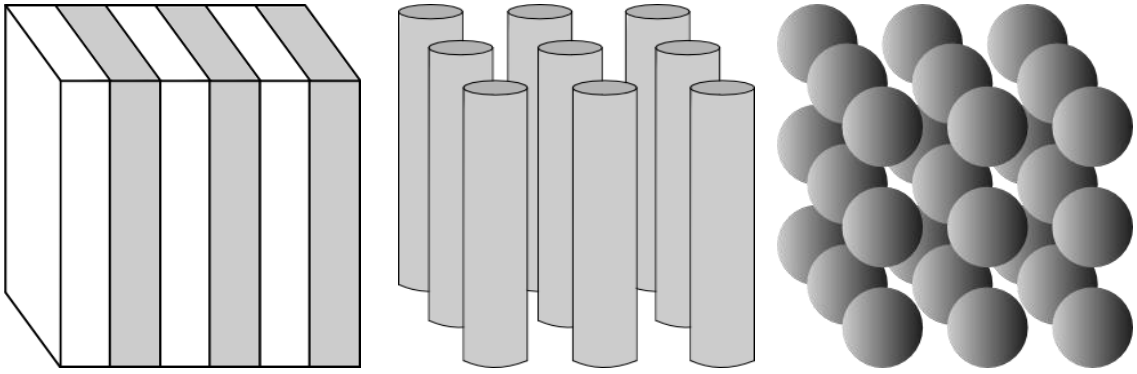

Figure 1.6 Three types of magnonic crystals regarding their dimensionality: one-, two-, and three-dimensional MCs respectively.

2. EXPERIMENTAL AND SAMPLE PREPARATION METHODS

In this chapter we describe the methods used in this thesis for the preparation of samples, their imaging and for measurements of static and dynamic magnetic properties.

2.1. Magnetron sputtering

In magnetron sputtering method, high voltage of few hundred volts is applied between anode and cathode to obtain a region with high density of ions and electrons. Permanent magnets are placed so that the magnetic field lines, which curve the trajectories of electrons, are aligned parallel to the target surface. The target is a source of sputtered material, mounted on the cathode. The induced spiral movement of electrons increases the probability of their collision with gas atoms and thus the ionization of the latter. The ions are then accelerated by the electric field and crash into the target, throwing out its atoms that are deposited on the substrate. The scheme of the setup used for magnetron sputtering is shown in Figure 2.1. Magnetic field, besides densifying the plasma near the target surface and thus increasing the rate of the deposition process, stop the secondary electrons ejected from the target which could otherwise hit the substrate and heat it up. The sputtering process can be performed with inert gas (i.e. argon) or reactive one. In the first case, the deposited layer consists of only target atoms, in the second case also chemical compounds generated in the reaction of the gas and the ejected atoms will be deposited. The advantage of magnetron sputtering is its high deposition rate and that is why it is often used in industrial applications. The disadvantage of the process is the non-uniform target wear because of plasma density difference in specific areas [11].

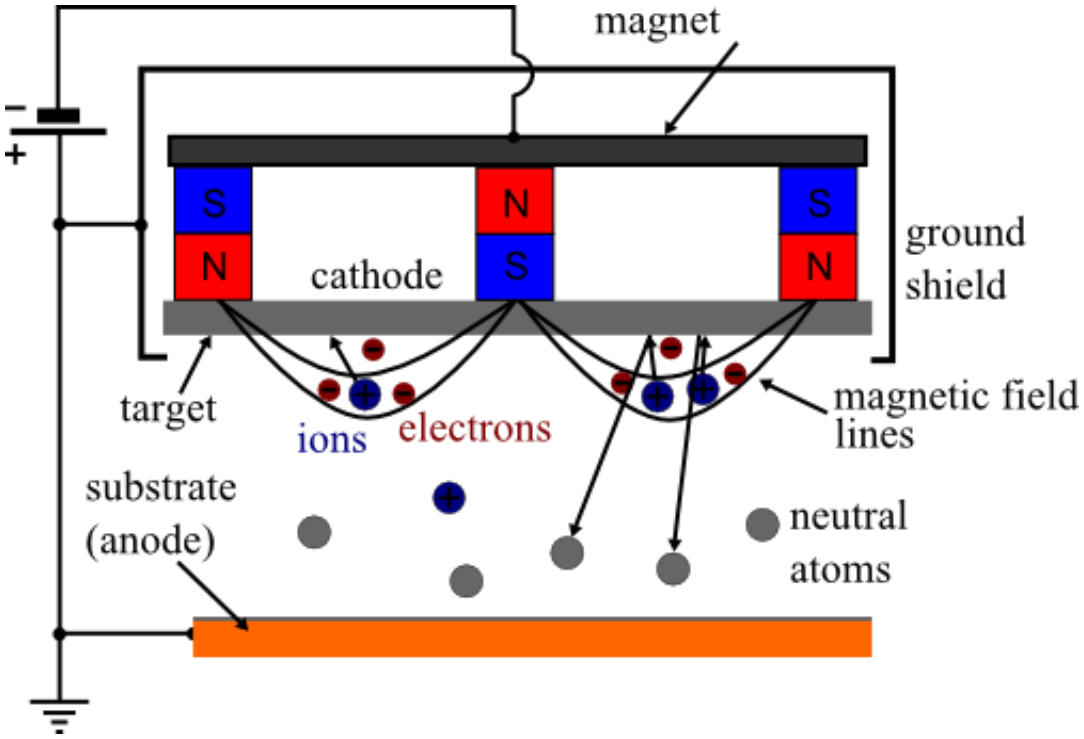

Figure 2.1 Scheme of setup used for magnetron sputtering. Based on [11]

2.2. Scanning electron microscope

Scanning electron microscope (SEM) is a technique used in imaging of structures topography and also in electron-beam lithography process. A simplified setup scheme is shown in Figure 2.2. Electron beam is created in electron gun through thermal emission using i.e. glowing filament from tungsten or LaB_6, through field emission from tungsten tip or using a combination of these two methods - through thermal field Schottky electron emission. Electrons are then accelerated with high voltage of 1-30 kV and shaped into beam thanks to the condenser lens. The objective lens is used to focus the electrons on a sample. Moreover, the beam is confined by the gap. As a result of electrons interaction with the sample, we can obtain signals of different types. SEM imaging usually employs secondary electrons. They come from atoms placed close to the sample surface. They are very numerous and the number of emitted electrons through collision with primary electron for high acceleration voltage can exceed one. The other type of emitted electrons are the backscattered ones. They form as a result of elastic scattering of beam electrons. There are less numerous than secondary electrons, but their advantage is a strong dependence of the intensity of this process on the atomic number of atoms in the sample. It allows distinction of phases from different elements.

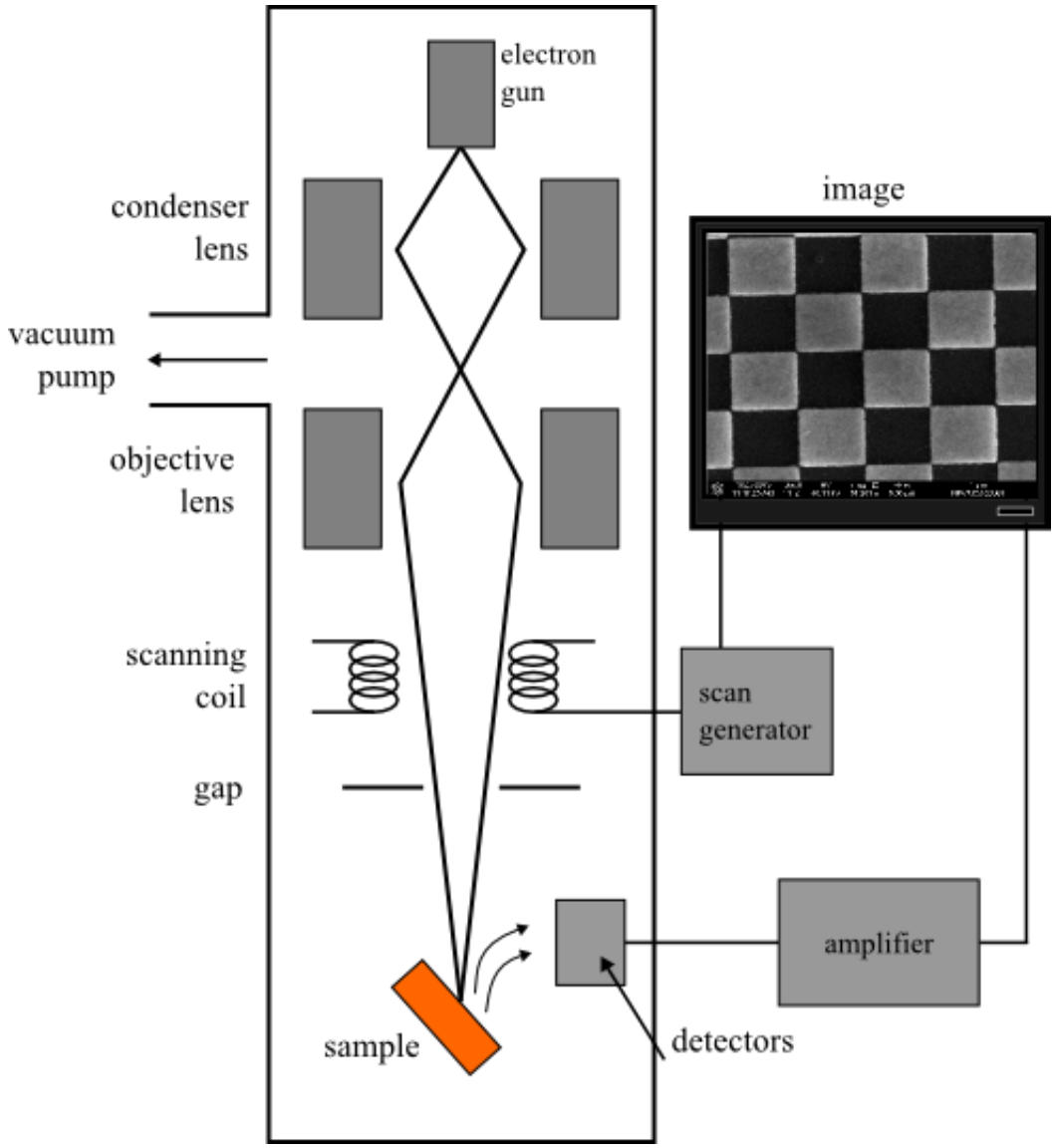

Figure 2.2 Simplified scheme of scanning electron microscope setup. Based on [11]

By using an electron beam it is possible to excite atoms. If an electron from an inner shell is ejected, another electron from a higher orbital falls into the lower one to fill the created gap. During this process a quantum of characteristic X-ray radiation is emitted. For transition between outer orbitals, quanta of visible photons can be radiated. Characteristic X-ray radiation can be emitted outside the sample or used for emission of electrons from the outer shield – Auger electrons. The probability of Auger electron and X-ray emission changes with the atomic number and that of Auger process is higher for lighter elements. It is worth mentioning that Auger electrons emission with conservation of their characteristic energy occurs only from the subsurface region (a few monolayers) of the sample. Both characteristic X-ray radiation and Auger electrons can be used to analyze chemical composition of the sample. Electrons

or electromagnetic waves emitted from the sample are collected by a proper detector. The primary beam is shifted by the scanning coil. In this way we can scan the sample surface line by line. Brightness of the corresponding pixels is determined by the enhanced signal from the detector and in this way the image is created [11].

The advantage of scanning electron microscopy is the possibility of imaging structures with a resolution of a few nm in a short time and a wide range of magnification. Moreover, the image obtained has a significant field depth. It is also possible to image the sample from different angles. The drawback of this method is the necessity of carrying out the process in vacuum. There are also problems with imaging non- or weakly conductive samples, which sometimes requires special preparation i.e. deposition of a conductive layer on them or the use of a low acceleration voltage which results in worse resolution.

2.3. Lithography

Lithography in nanotechnology is a method of manufacturing structures of nanometric dimensions. It is used i.e. in production of integrated circuits, mass storage etc. This technique uses emulsion (resist) deposited on a sample surface which change its properties under influence of light, electron beam, ion beam or X-ray radiation. Thanks to the lift-off method it is possible to create structures on samples of a thin deposited film. Depending on the size of the elements, electron-beam lithography (EBL) or direct laser lithography can be used. Both methods are described in the following sections.

2.3.1. Electron-beam lithography

In electron-beam lithography a beam of electrons in the scanning electron microscope is used to illuminate a sample covered with a resist. Thanks to SEM we are able to create structures with high resolution. Significant limitations are the width of the beam, which can be focused to a diameter of a few nm, and the process of electron scattering with the emulsion. The electron beam can be precisely deflected in a range of 800 μm maintaining good focus and beam shape. During the process it is necessary to have high vacuum in the microscope chamber, as insulation from the electromagnetic fields, which could influence the position of the beam. To obtain structures in the range of tens of nm, the system should be equipped with a good vibration isolation system. The main disadvantage of this method is its long exposure time. That is why in industry it is

mostly used for mask fabrication, which can be used for a much faster photolithography method.

The resist consist of a resin, which provides mechanical stability, photosensitive substances and a solvent which influences the density of emulsion. The main two types of resist are positive and negative. In the positive one, illuminated regions become more soluble in the developer. As for the negative resist, irradiated emulsion polymerizes and becomes more difficult to dissolve. Because of that, developer removes all the resist except the exposed one. This process is shown in Figure 2.3.

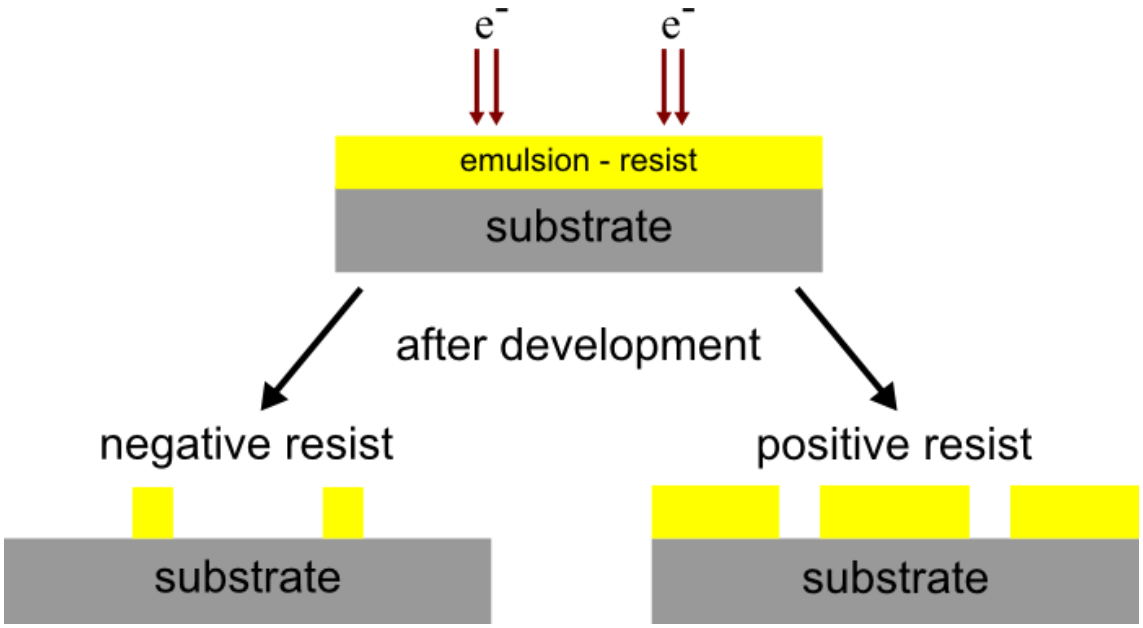

Figure 2.3 Schematically illustrated effects of exposition and developing the negative and positive type of resist.

Resist can be deposited with a spin coater. On an earlier cleaned substrate we drop resist and then start the stage rotation. Spin coaters for emulsion deposition are equipped with a vacuum system for sample holding. The thickness of resist depends on the rotation speed and the density of emulsion. To preserve the defect free structures, the whole process takes place in a clean room. After deposition, the sample is baked to harden the resist and improve adhesion to the sample surface. It helps also with emulsion sensitivity for changing its properties by electron beam.

The process of thin films patterning can be realized by the lift-off method or by etching. In the first case, the resist is used as a template. Structures on the resist are exposed to the electron beam and development process removes illuminated regions (for positive resist). After that the material is deposited on uncovered underlying material

and the remaining resist. Finally, the emulsion is removed and the sample with the material deposited in places previously exposed to electrons is obtained. In the second method, the resist is used as a mask. After exposition and development of the resist, the etching of uncovered material (and the remaining resist) is performed i.e. using ions. So after the removal of the whole resist we obtain cavities at the previously illuminated sites. Both methods are illustrated in Figure 2.4.

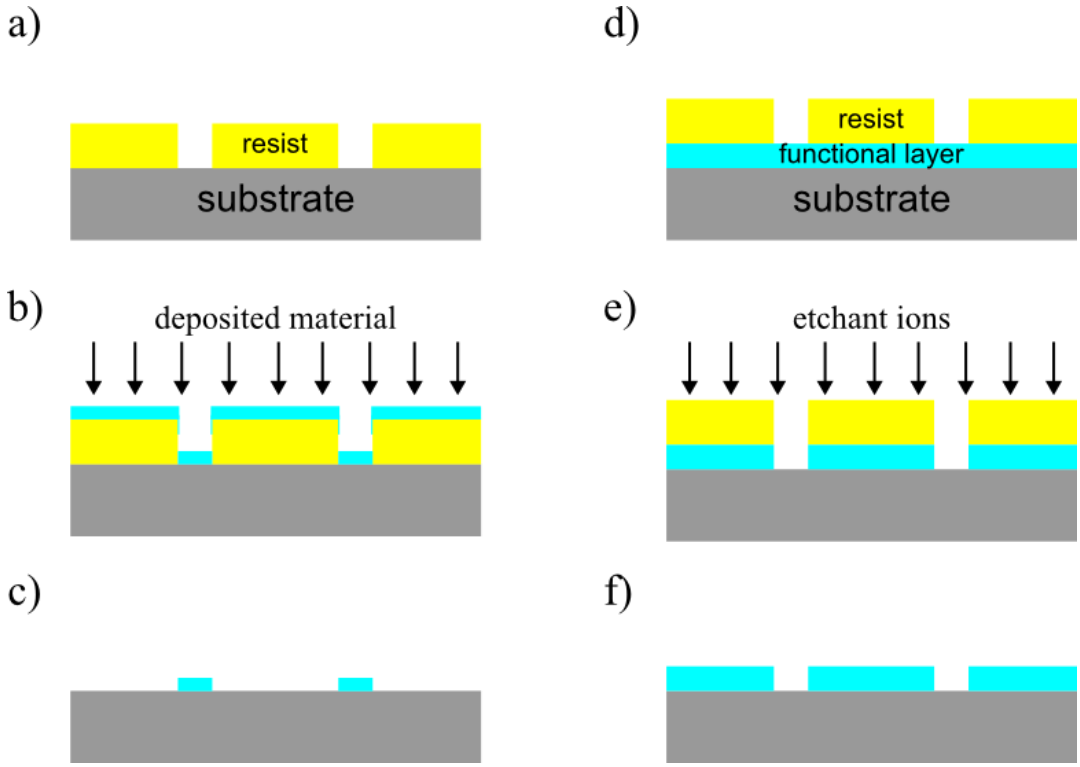

Figure 2.4 Schematically illustrated methods of patterning with lift-off (a-c) and ion etching (d-f) using exposed and developed resist.

In electron-beam lithography one of the factors that can affect the accuracy of elements produced is the proximity effect. It refers to size variation of patterned elements because of the presence of other exposed regions in close vicinity. As a consequence, this effect limits high resolution of EBL and can influence the size and shape of the structures. For example, common effects are: rounded corners, changed width of lines and gaps or even merging of closed packed elements. Proximity effect is caused by backscattered and secondary electrons that appear as a result of electron beam interaction with the resist-coated substrate. It is thus dependent on the voltage accelerating the electrons, the material, thickness of the resist and the type of substrate. The intensity distribution of exposure is a Gaussian shaped, which is schematically shown in Figure 2.5. A few methods have been proposed to compensate for the proximity effect. It is

possible to adjust the electron beam dose to the density of the elements or to take into consideration changes in the features dimensions and compensate it in advance in the design of the exposed structures. Proximity effect is weaker for higher acceleration voltage, thinner resist and substrate with lower atomic number. Some of the lithography software offer correction of this effect by dividing the structures into smaller elements and adjusting the dose of electrons [21].

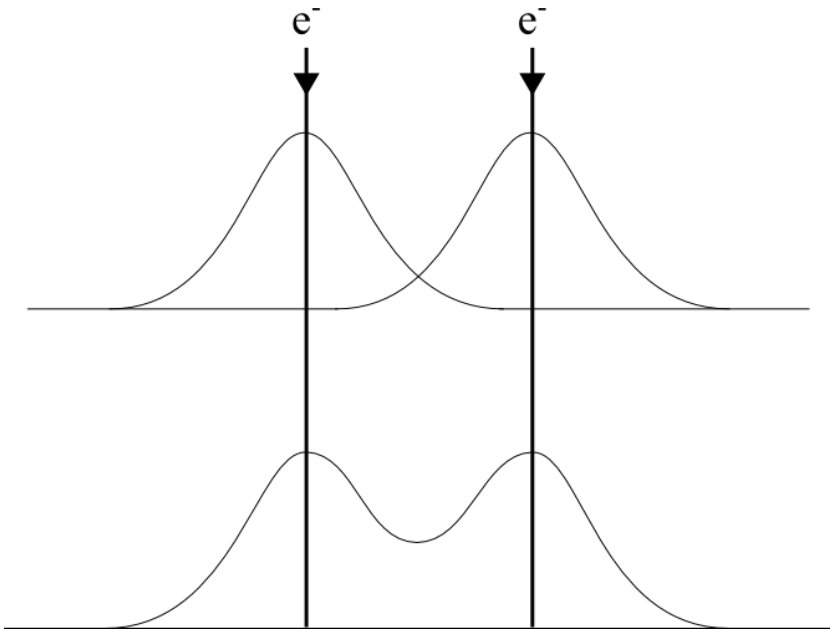

Figure 2.5 Schematically illustrated Gaussian shaped intensity distribution of exposure to two electron beams (upper picture) and the sum of this intensity (lower picture) where the proximity effect in between is visible

In EBL, the easiest way to structure the sample with lift-off method is to use only one layer of a resist. It is shown in Figure 2.6. Although there are some disadvantages of this approach. One of them is the possibility of spoiling the pattern with the so-called "garden fences" which can be seen in Figure 2.6 in point e) and in Figure 2.7. It can occur because deposited material settles not only on the top of the resist and, through the window in the emulsion, material below it but also on the sides of the exposed and developed resist (see Figure 2.6d). After the lift-off procedure, some of this material may stay on the structures. Another problem may occur with closely packed elements. During the lift-off it can be difficult for the solvent to dissolve completely the resist between these structures and remove unwanted deposited material so out elements can merge. The solution to this problem might be using a double layer of resist: more sensitive at the bottom and less sensitive at the top (see Figure 2.8). Thanks to this, after exposition and development we can obtain undercut (visible in Figure 2.8c) which

prevents the formation of “garden fences” and also help with the lift-off because the solvent has more space to get under the material deposited on the resist and removes it easier. The drawback of using double resist layer is deterioration of the resolution. When structures are too close to each other, the bottom resist can became too narrow and detach from the substrate.

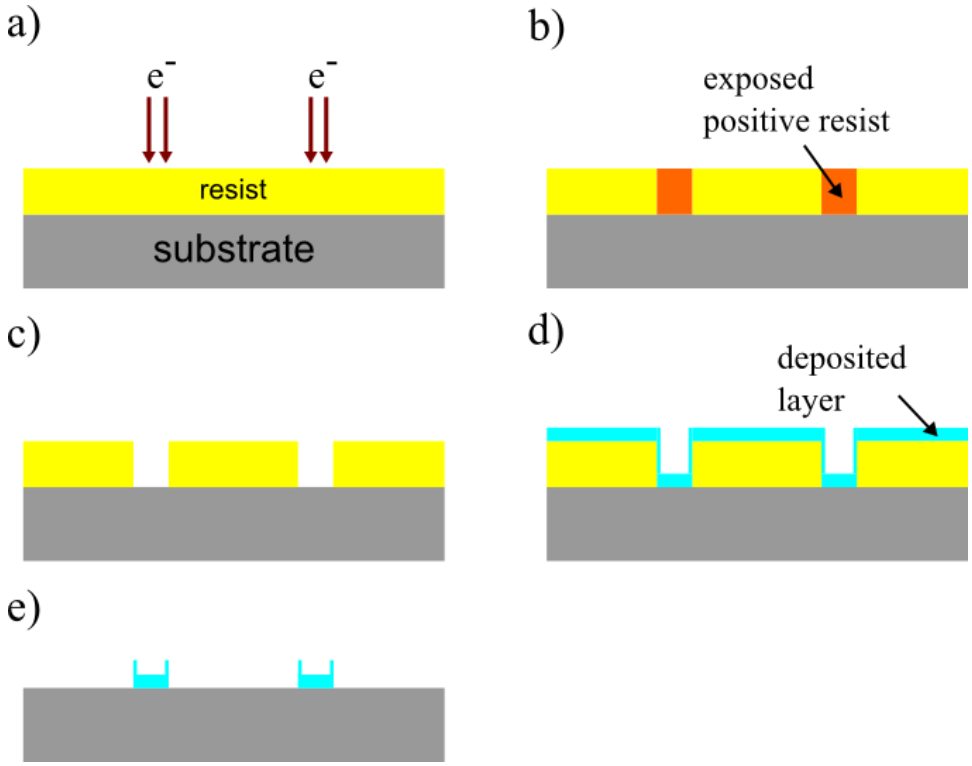

Figure 2.6 The following steps of lift-off sample structuring with one layer of a resist: sample exposition to the electron beam (a), positive resist after exposition (b), resist after development (c), sample after layer deposition (d) and sample after removal of the remaining resist (e).

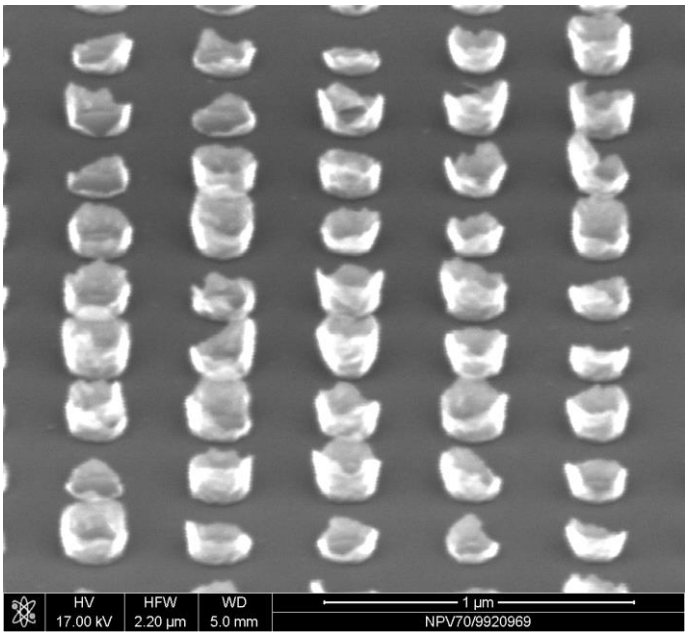

Figure 2.7 SEM image of dots array showing the "garden fences" effect.

Sometimes, after the lift-off process some of the resist can still stay on the substrate. It is possible to efficiently get rid of it using for example a plasma cleaner. In plasma cleaning, gas under low pressure (fraction of mbar) is ionized in a chamber with the sample using a high frequency voltage (kHz-GHz). Plasma reacts with the sample surface and the nature of this reaction depends on the factors like frequency of the voltage exciting atoms, type of ionized gas, its pressure (determined by gas flow), sample material and time of the process. The ions (particularly of oxygen and hydrogen) by reacting with molecules on the surface cause their decay and create new compound with relative high vapor pressure, which is easier desorbed from the sample surface. Moreover, UV radiation generated by the atoms excitations also can cause breaking of chemical bonds, especially in organic contaminants. It is also possible to use noble gases like argon. They are inert, but their ions can clean the sample surface through impacts with it.

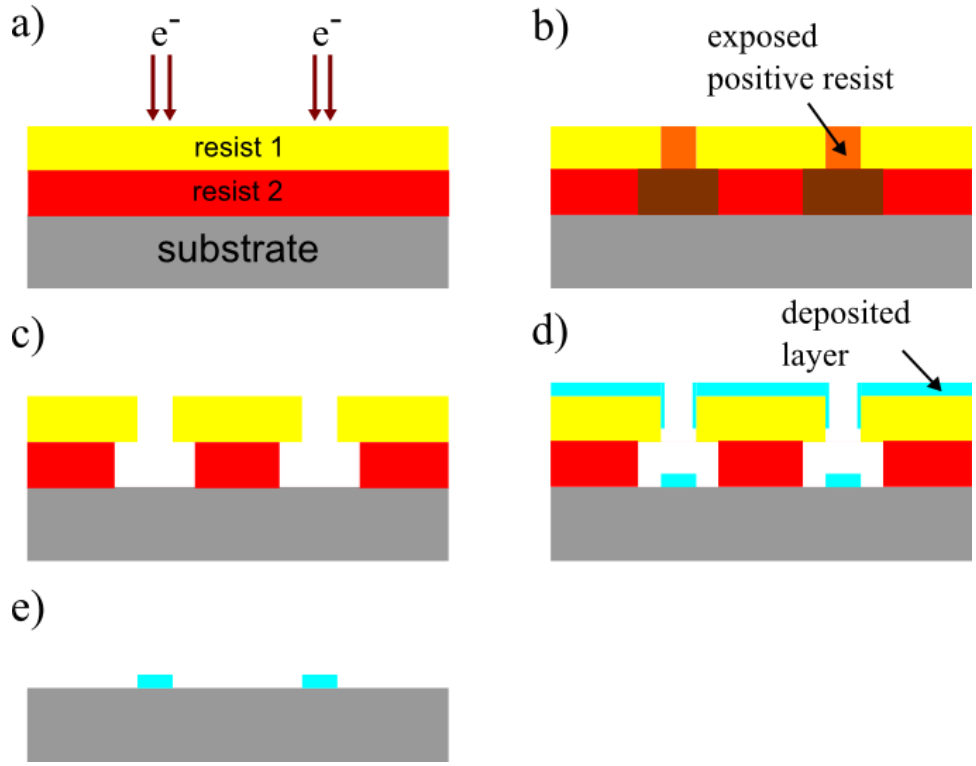

Figure 2.8 The following steps of lift-off sample structuring with two layers of resists (more sensitive at the bottom and less at the top): sample exposition to the electron beam (a), positive resists after exposition (b), resist after development with visible undercut (c), sample after layer deposition (d) and sample after removal of the remaining resist (e).

2.3.2. Direct laser lithography

Direct laser lithography (or direct laser writing) is a type of maskless photolithography. The key advantage of this solution (in comparison to the conventional photolithography) is ability of quick change of the pattern without the necessity of making a new photomask. In this method the photoresist is illuminated directly with a focused beam of light. The principles of sample preparation before exposure are similar to those for the electron-beam lithography. After cleaning and drying the substrate, photoresist is applied using a spin coater and then sample is baked. It has to be performed in a clean room. Photoresist is an emulsion which is sensitive to light (usually from UV range). Because of that, the whole process must be additionally done under yellow light. Just like in EBL, there are (mainly) positive and negative photoresists with analogous effects after exposure (see Figure 2.3 for EBL). The resolution of this method is sub-µm. Despite that, its advantages in comparison to the electron-beam lithography are large scan area (up to 6” with the equipment used for this thesis) and much faster speed of the process. Moreover, no vacuum is required. After development, the sample treatment is the same as for EBL, i.e. we can use lift-off technique or etch the pattern.

2.4. Profilometer

To determine the thickness of resist layers, a profilometer DektakXT made by Bruker company was used. The principle of its operation is that on the surface of the sample a probe with a diamond tip is placed and moves with a determined speed, force of press and length of the scan line. The vertical position of the probe is measured electromechanically, using a differential transformer. As a result we obtain a plot of changes in the sample height as a function of position. Schematic cross section of a sample and the corresponding profile obtained are shown in Figure 2.9.

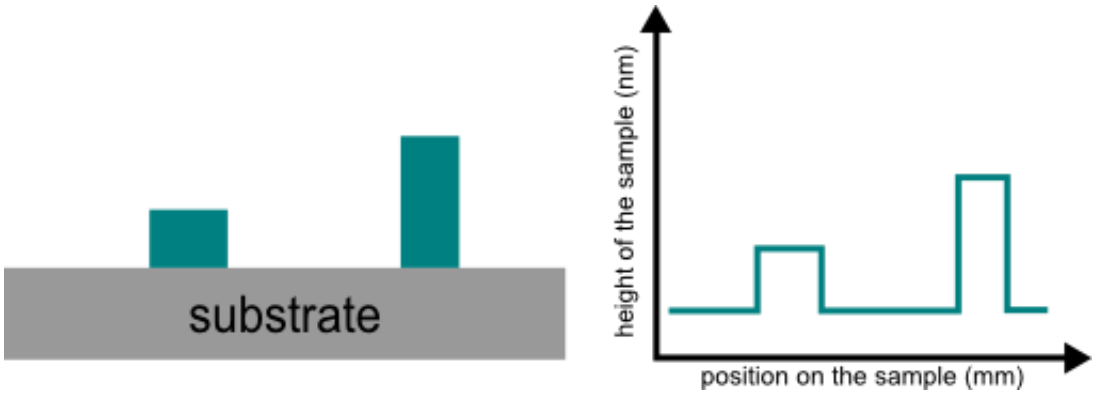

Figure 2.9 Schematic cross section of a sample and its obtained height profile

Depending on the need, probes with different radius of its tips curvature can be used, because smaller tips allow better resolution of measurement. Moreover, for samples with different stiffness, we can set other forces in which probes act on the surface. In standard configuration this value is between 10 and 150 μN. Profilometers are widely used to measure the thickness of layers and roughness of surfaces. Their advantages are high resolution (up to single nm), easy operation and short measurement time.

2.5. Vector Network Analyzer Ferromagnetic Resonance

In standard Ferromagnetic Resonance (FMR) technique, the excitation of magnetic material is excited in a microwave cavity in which sample is excited only at one frequency by a resonator. In this thesis a Vector Network Analyzer Ferromagnetic Resonance (VNA-FMR) and coplanar waveguides (CPWs) are used to study broadband dynamic magnetic effects.

2.5.1. Coplanar waveguides

A coplanar waveguide (CPW) consist of three metallic stripes: one inner signal line *S* and two outer ground lines *G*, all parallel to each other. At the one end of the CPW used

there is a taper part to which the probe can be attached, while the second end is shorted. The *S* line carries the signal current which then splits into two *G* lines and flows in the opposite directions. Because of that an oscillating field h_{rf} is created around each line, which causes precession of the spins in the material which is below or above the CPW. The distribution of this field is strongly dependent on the geometry of the antenna [15]. Figure 2.10 presents a schematic cross section of a coplanar waveguide and the distribution of the field lines around the *S* line. The k-vector of excited wave depends on the geometry of the CPW used. In measurements of the spin waves propagation with two CPWs, one of them is used to excite and the other to receive the signal, because precessing spins can induce voltage in it.

An important parameter that characterizes a coplanar waveguide is impedance. In general, if two electrical systems with different values of this parameter are connected, scattering of electromagnetic waves takes place. To minimize this effect, the impedances of these systems have to be matched. The standard value is 50 Ω. It also holds for VNA equipment and microwave cables. Because of that, the desired impedance of CPW also has to be of 50 Ω. For high frequencies, the influence of ohmic resistance on impedance value is irrelevant. It has been shown [16] that it mainly depends on the ratio of the width of the signal line and the gap between this line and the ground line. Therefore it is possible to change the cross section dimensions of the CPW while maintaining the impedance matching.

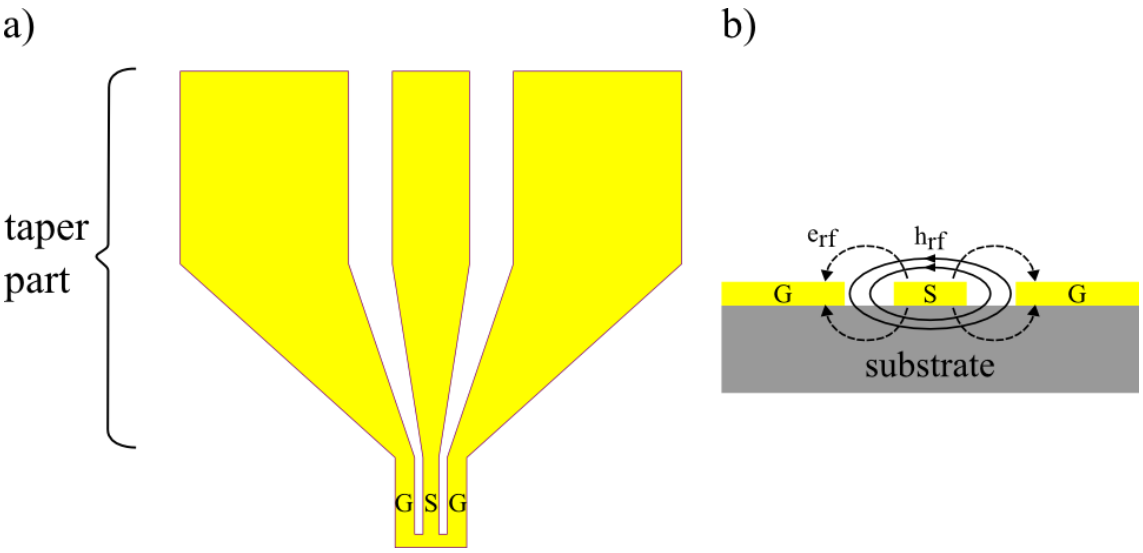

Figure 2.10 The schematic CPW with highlighted taper part (a) and CPW lines cross section on the substrate (b). The lines are labeled as S – signal line, and G – ground line. The lines of magnetic h_{rf} (full lines) and electric e_{rf} (dashed lines) are shown only for S line.

2.5.2. Vector Network Analyzer

A Vector Network Analyzer (VNA) can be used as both a source of microwave signal and a detector. It has two ports and generates a sinusoidal high frequency signal from 10 MHz up to 40 GHz, which in combination with CPW connected through probes and microwave cables can be used to excite the magnetic material. The VNA is able to measure both amplitude and the phase of the voltage, from which scattering parameters (S-parameters) for two ports (1 and 2), defined as:

$$\hat{S}_{11}(\omega) = \frac{\hat{V}_{refl}(\omega)}{V_0(\omega)}$$
$$\hat{S}_{12}(\omega) = \frac{\hat{V}_{trans}(\omega)}{V_0(\omega)} \qquad 2.1$$

can be extracted [16]; $V_0(\omega)$ is the incident voltage, $\hat{V}_{refl}(\omega)$ the reflected voltage, measured at the same port as the incident and $\hat{V}_{trans}(\omega)$ the transmitted voltage, from the second port. Therefore $\hat{S}_{11}$ is the reflection and $\hat{S}_{12}$ the transmission coefficient. Analogically we can define the parameters $\hat{S}_{22}$ and $\hat{S}_{21}$ for port 2. The dependences between different signals and the corresponding S-parameters are shown in Figure 2.11.

One of the methods to obtain a better signal-to-noise ratio is the difference method. A reference measurement S_{ref} is taken in a reference field and then subtracted from the actual measurement S_{act}, so as a result we obtain a difference signal:

$$\Delta S = S_{act} - S_{ref}. \qquad 2.2$$

After such a procedure, the signals from the connections, cables etc. are effectively eliminated from the measurement. Preferably, the reference field should be applied in different orientation than during the measurement and if measurement setup does not allow changing the field direction, it should be high enough to obtain the resonance line above the measured frequency range. If it is also not possible, it should be at least chosen to influence measured signal as little as possible and not to overlap frequency peaks [15].

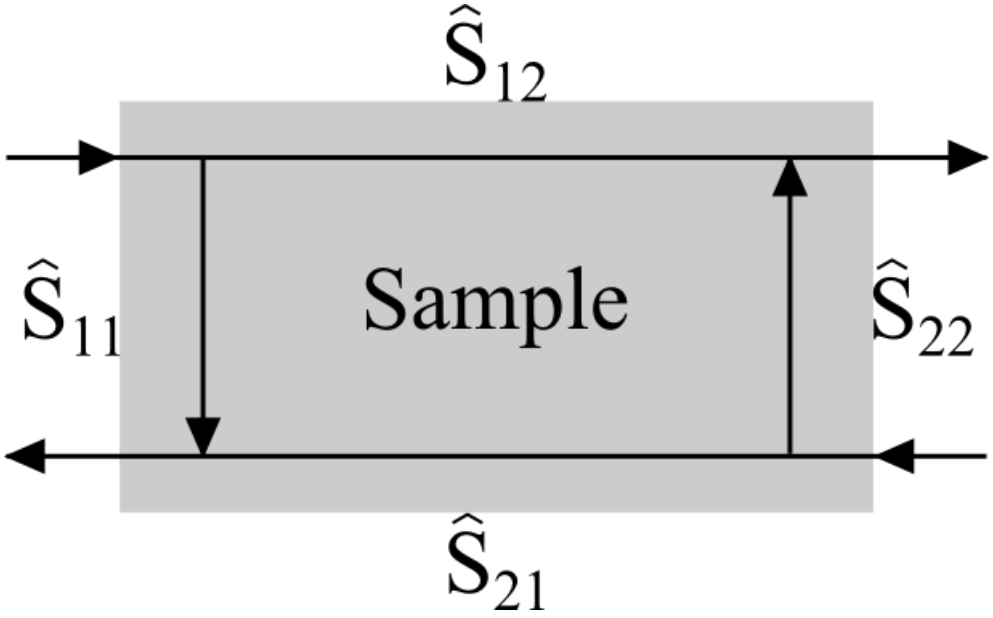

Figure 2.11 Diagram of the scattering parameters

2.6. Brillouin Light Scattering

Brillouin Light Scattering (BLS) is an optical experimental technique which can be used to investigate spin wave excitations in the GHz regime. Important advantages offered by this method, in comparison to microwave spectroscopy, are: the possibility of measurements of spin waves spectrum with different, tunable wave vectors **k**, the possibility of detecting of high-amplitude magnons which can be excited by an applied external microwave field as well as low-amplitude spin waves from thermal excitations and also high spatial resolution which depends on the size of the laser beam spot [22]. BLS is based on inelastic scattering of photons. Incident photon of frequency ω_I and momentum q_I interact with a magnon (ω, q) and loses part of its energy for magnon creation (Stokes scattering) or gains it through magnon annihilation (anti-Stokes scattering). Because of that, the momentum q_S and the frequency ω_S of the scattered photon are shifted (Brillouin shift) by values

associated with the magnon. The diagram of this process is shown in Figure 2.12. During the measurement, monochromatic laser light has to be used and the frequency of scattered light is collected. To distinguish between these small frequency differences, a Fabry–Pérot interferometer is used. Moreover, by changing the angle θ between the incident light and the sample surface, the in-plane component of the wave vector is varied according to:

$$k = \frac{4\pi}{\lambda_L} sin\theta \qquad 2.3$$

where λ_L is the wavelength of the laser. By sweeping this angle it is possible to obtain the dispersion relation of the spin waves.

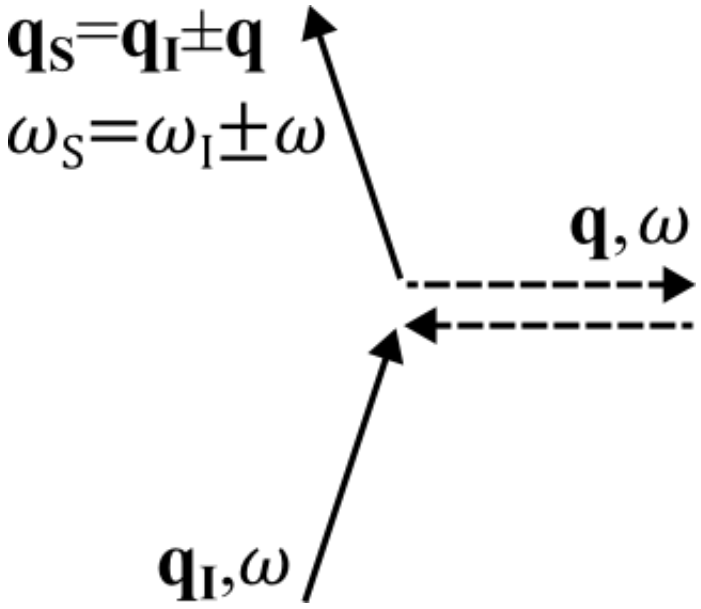

Figure 2.12 Inelastic scattering process of a photon with a spin wave [22]

2.7. Magneto optical Kerr effect

Magneto optical Kerr effect (MOKE) for the linearly polarized light appears as a rotation of the polarization plane after its reflection from a surface of magnetic material because of the interaction with electrons. There are different configurations of measurement, depending on the relative orientation of the magnetization **M,** electric field vector **E** of the light and the plane of the sample. Polar MOKE, the strongest of these effects, occurs when there is out-of-plane **M** compound which is perpendicular to **E** (direction of polarization). Electric field from linearly polarized light causes vibration of electrons in the direction of **E**. Because of that, reflected beam has the same polarization plane as the incident light. However because of the Lorenz force, additional vibrations occur in the direction perpendicular to **M** and **E**. As a result there is another polarization, perpendicular to the primary polarization, which causes its rotation.

The strength of observed rotation is proportional to the magnetization of measured area, which is limited by the beam size and depth of light penetration into the material examined. This effect is the strongest when light beam is perpendicular to the sample surface. The P-MOKE configuration is shown in Figure 2.13. Another configuration is the Longitudinal MOKE (L-MOKE) in which **M** lies in the plane of the sample and parallel to the incidence plane. In the Transversal MOKE (T-MOKE) magnetization is also in-plane of the sample but perpendicular to the plane of incidence. In this case, there is no change in light polarization because there is no Lorentz force (**E**∥**M**) or the component which is induced has the same polarization direction as the incident one. Because of that, instead of polarization, a change in the light intensity is observed (Kerr reflectivity). In L-MOKE and T-MOKE light has to be reflected at some angle to the normal of the surface [23].

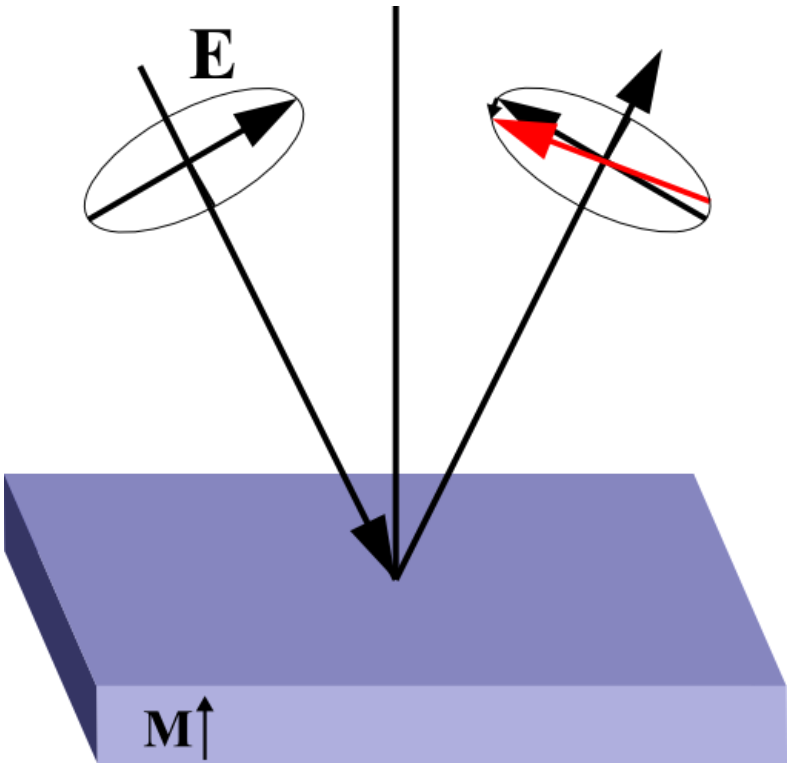

Figure 2.13 Polar configuration of magneto optical Kerr effect

2.8. Magnetic force microscope

Atomic force microscope (AFM) is a technique which allows us to measure a surface of a sample by scanning a sharp tip over it. The tip is placed at the end of a cantilever which is usually few hundreds of μm long. The force which is acting between the tip and the sample surface (mostly van der Waals forces) causes the cantilever to bend

or twist. A sensitive detector measures this deflection while probe scan the sample surface. Obtained data allows creating a topographic map of the measured surface even with resolution on the order of fractions of a nanometer.

AFM can operate in different modes. In contact mode tip is moved over the sample surface and the image is created using either cantilever deflection or the feedback signal which moves the scanner to keep the force between the tip and the surface at the same level. In non-contact mode probe is in some distance (few to tens of nm) from the surface and oscillate with its eigen frequency. Because of interactions with the sample the frequency (or oscillations amplitude) is changing which is used to image the surface contour. The third mode is tapping mode where probe oscillate much closer to the sample surface and scan it by "tapping" the surface. Here also the change of amplitude is used to create the topography image.

Magnetic force microscopy (MFM) is a technique closely related to the atomic force microscope, although used tip is covered with ferromagnetic material which allows imaging the differences in magnetic force acting on it in different points of the sample surface. The schematic principle of operation is shown in Figure 2.14. In the contact mode short-distance van der Waals interactions dominate although over some height from the surface start to dominate long-distance interactions between the magnetic moment of the tip and stray field from the sample. That is why the usual MFM scan requires first scanning at the close distance in the contact mode to measure the topographic profile after which tip is lifted to a bigger distance and from the second pass, considering the profile line, magnetic signal is obtained. This technique can be used for example to image the magnetic domains in the sample.

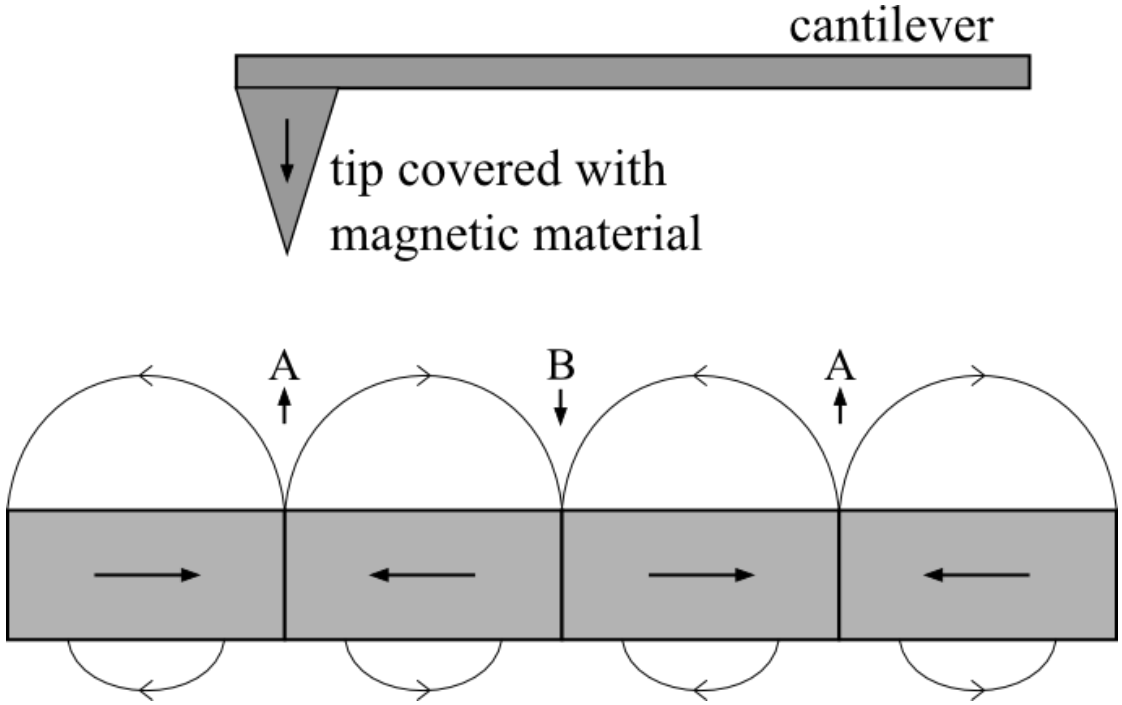

Figure 2.14 Schematic principle of MFM operation. Sample is magnetized in plane, which creates stray field over surface vertically up (A) and down (B). The tip is magnetized downward, so it is repelled in a place A and attracted in B. The magnetic field lines are shown as arrows. Based on [11].

3. OBJECT OF RESEARCH

In this chapter the subjects of study, which are arrays of periodic and quasiperiodic $Ni_{80}Fe_{20}$ stripes separated by air gap are presented. The principle of these structures formation is explained. The sample preparation procedure is also addressed here.

3.1. Periodic and quasiperiodic $Ni_{80}Fe_{20}$ stripes arrays

The subjects of study in this thesis are one dimensional magnonic crystals consisting of arrays of two types. The first is periodic structure of 350 nm wide $Ni_{80}Fe_{20}$ (Permalloy – Py) stripes separated by 100 nm air gaps. The other is quasiperiodic structure, which was build using Fibonacci sequence from the same material blocks A ($Ni_{80}Fe_{20}$) and B (air). This is explained in Figure 3.1. The further structure is created by adding two previous ($F_N = F_{N-1} + F_{N-2}$). In other words, Fibonacci inflation rule is used where next sequence is created by changing materials from previous one by a rule:

$$B \rightarrow A, \qquad A \rightarrow AB. \tag{3.1}$$

As a result, quasiperiodically ordered structure of 350 nm and 700 nm width Py stripes separated by 100 nm air gap is created. In both cases, thickness of Py is 30 nm and stripes are few μm long. The cross-section of both sequences is shown in Figure 3.2.

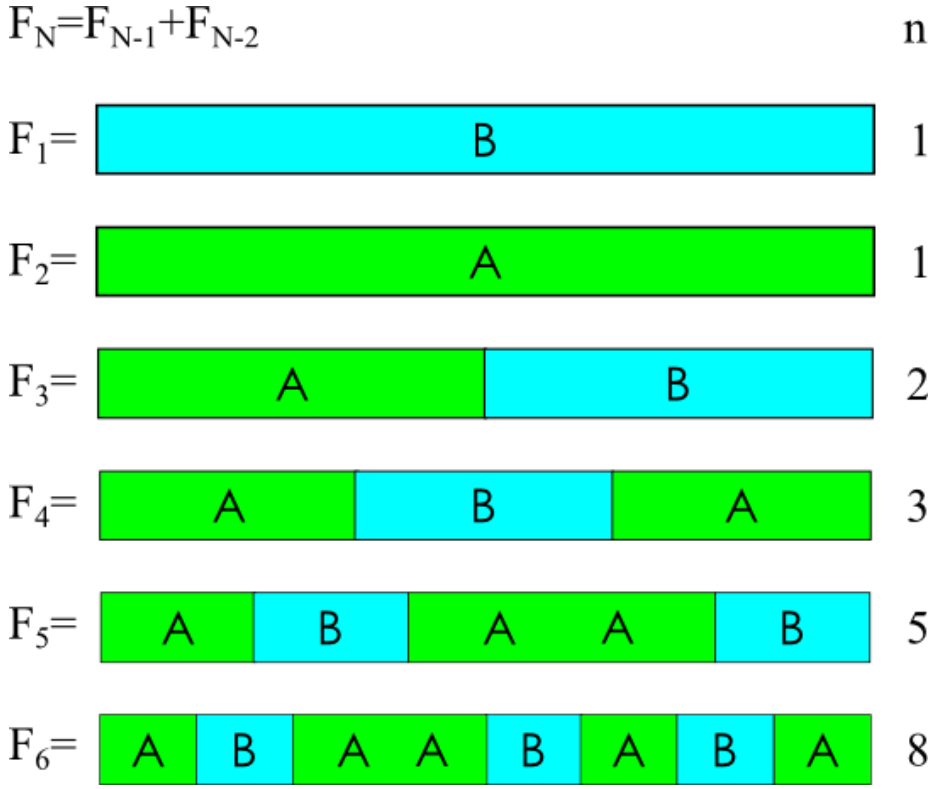

Figure 3.1 Formation of the stripes array using Fibonacci sequence. Materials are: $Ni_{80}Fe_{20}$ (A - green) and air (B - blue).

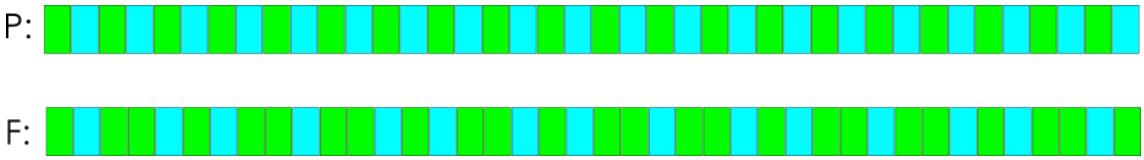

Figure 3.2 Cross-section of investigated structures for n=40 elements consisting of $Ni_{80}Fe_{20}$ stripes (green) separated by air (blue). P – periodic sequence and F – Fibonacci sequence.

3.2. Samples preparation

To prepare samples, two lithography techniques were used: electron-beam lithography and direct laser lithography. These methods are complementary, because EBL, providing much higher resolution, was used for preparation of magnetic stripes, and direct laser lithography, which is much faster technique and can be used for large areas, was employed for coplanar waveguides and antennas fabrication.

The steps of stripes array fabrication are as follow:

- Cut of 10 x 10 mm silicon (100) substrates. Resistivity $> 4\ k\Omega$.
- Substrate cleaning in clean room conditions. First mechanical cleaning using clean room wipers and isopropanol. Then putting the substrate in three beakers with separately acetone, trichloroethylene and isopropanol in ultrasound bath, 5 minutes each. After that, drying using nitrogen and heating on a hot plate for 1 minute at 170 ^{o}C.
- For two resist layers, first layer: coating with methyl methacryllate (MMA) 8.5 positive resist using spin coater at rotational speed between 1000 and 6000 rpm for 60 seconds and baking for 90 seconds on a hot plate at 170 ^{o}C.
- Coating with polymethyl methacrylate (PMMA) 950K positive resist using spin coater at rotational speed between 1000 and 6000 rpm for 40 seconds and baking for 15 minutes on a hot plate at 170 ^{o}C.
- Structures exposition with electron-beam lithography.
- Resist development in methyl isobutyl ketone (MIBK, 1:3 with isopropanol) for 56 seconds, then rinsing in two glasses with isopropanol for 15 seconds each and drying with nitrogen.
- Deposition of 30 nm $Ni_{80}Fe_{20}$ using magnetron sputtering method.
- Lift-off process using acetone and ultrasound bath and drying with nitrogen.
- Removing the residues of resist with plasma cleaner for 5 minutes (air pressure 0.5 mbar)

After obtaining the structured magnetic film, coplanar waveguides or antennas were fabricated according to the following steps:

- In some cases: deposition of 30 nm Al_2O_3 using magnetron sputtering method to provide electrical isolation between the CPW and the magnetic film (magnonic structure).
- Sample cleaning with acetone and isopropanol, drying with nitrogen and heating on a hot plate for 1 minute at 100 ^{o}C.
- Coating with 3510 positive photoresist using spin coater at rotational speed between 1000 and 6000 rpm for 60 seconds and baking for 1 minute on a hot plate at 100 ^{o}C.
- Structures exposition with direct laser lithography.
- Photoresist development in AR 300-35 (1:1 with deionized water) for 20 seconds, then rinsing in two glasses with water for 15 seconds each and drying with nitrogen.
- Deposition of 90 nm Al using magnetron sputtering method.
- Lift-off process using acetone and ultrasound bath and drying with nitrogen.

4. OPTIMIZATION OF THE FABRICATION PROCESS

In this chapter optimization process of structures fabrication is presented. In the first section electron-beam lithography, used for magnetic films structuring, is addressed. In the second section optimization process of coplanar waveguides by direct laser lithography is described.

4.1. Optimization of magnetic structures fabrication by electron-beam lithography

In this section optimization of magnonic crystals fabrication using electron-beam lithography is described. It includes determination of resist thickness for different rotational speed during spin coating process, correction of proximity effect and selection of resists configuration and electron dose.

4.1.1. Resist thickness

The first step to optimize the fabrication of structures using the electron-beam lithography is to determine the thickness of resists as a function of rotational speed used during the spin coating process. The emulsions used were: PMMA 950K 1.5%, MMA 8.5 2.5% and MMA 1.5%, all diluted in a suitable thinner. To perform the thickness measurement, samples were coated with resist at different rotational speeds: 2000, 4000 and 6000 rpm. Time of the spin coating process was not changed and for PMMA it was 40 seconds and MMA - 60 seconds. On so prepared samples some simple structures were exposed with electron beam of dose high enough to remove resist during development and create window in the emulsion up to the clean substrate. The resist thickness was measured using a profilometer. The results for PMMA 950K 1.5% are shown in Figure 4.1 and the equation of the curve approximating this dependence is:

$$y = 200 * e^{-\frac{x}{1200}} + 93, \tag{4.1}$$

where *y* is the resist thickness in nm and *x* is the rotational speed in rpm. For MMA 8.5 2.5% resist, results are shown in Figure 4.2, and the equation is:

$$y = 116 * e^{-\frac{x}{1280}} + 67, \tag{4.2}$$

and for MMA 8.5 1.5% this dependence is shown in Figure 4.3 and described by:

$$y = 79 * e^{-\frac{x}{1040}} + 39. \tag{4.3}$$

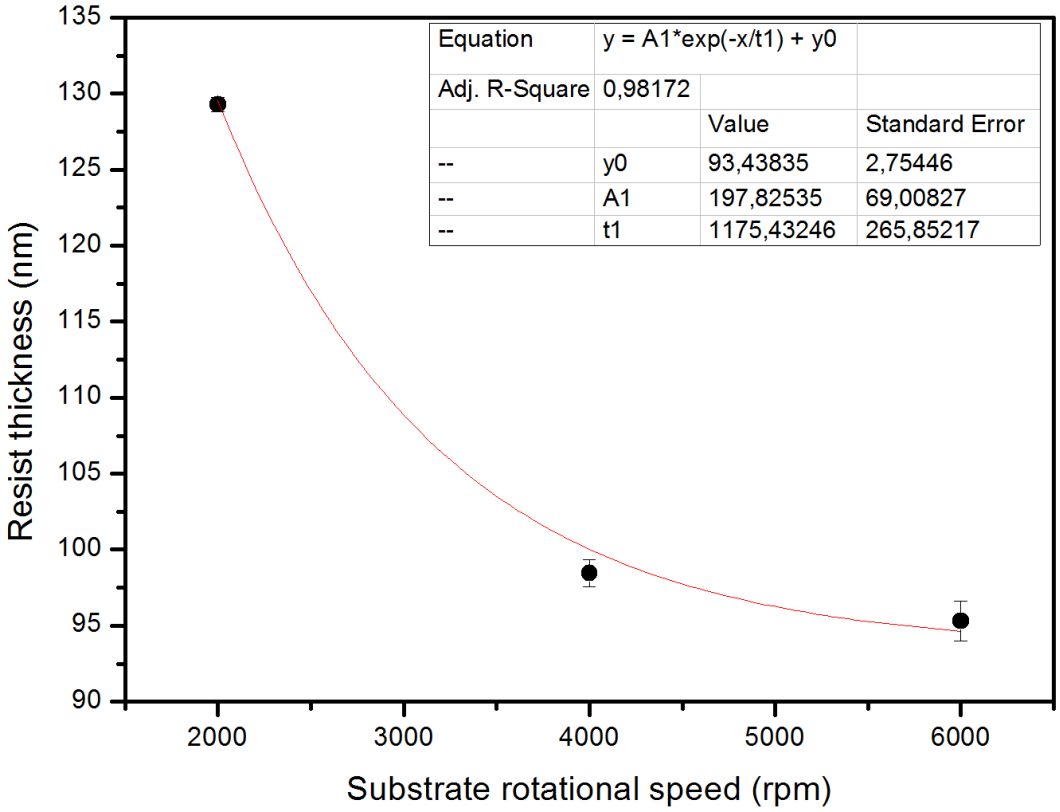

Figure 4.1 PMMA 950K 1.5% resist thickness as a function of substrate rotational speed.

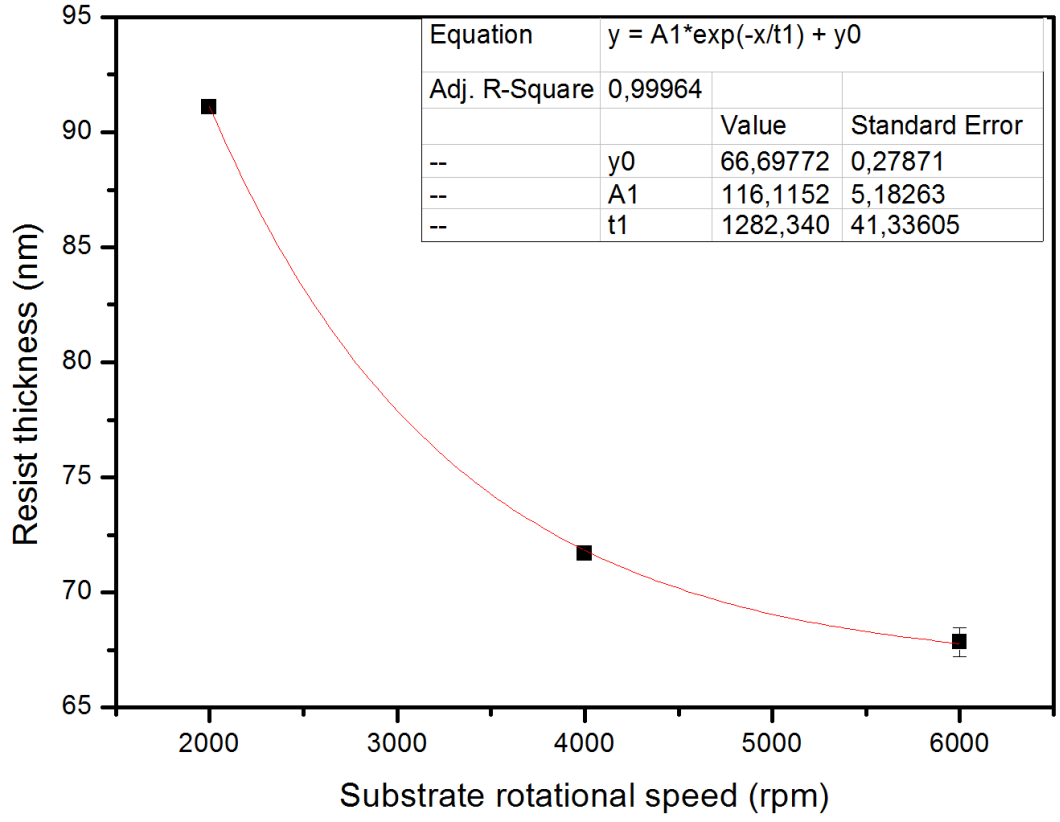

Figure 4.2 MMA 8.5 2.5% resist thickness as a function of substrate rotational speed.

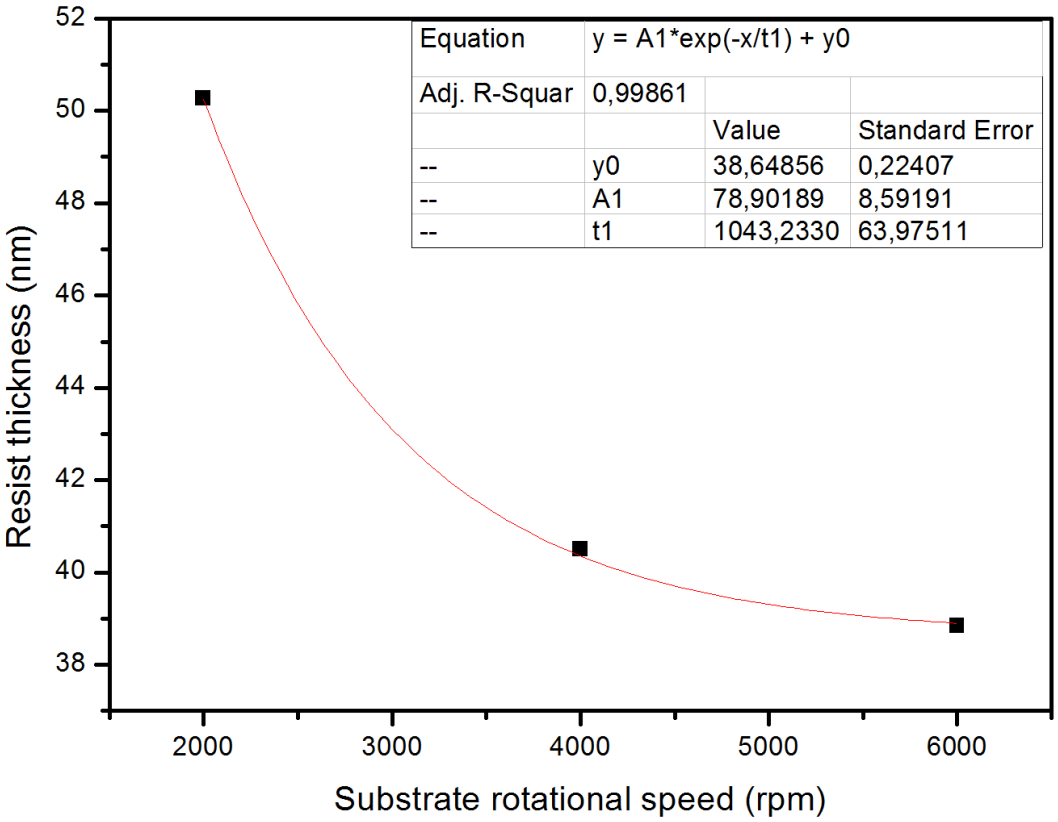

Figure 4.3 MMA 8.5 1.5% resist thickness as a function of substrate rotational speed.

4.1.2. Proximity effect correction

To compensate for the proximity effect, a software correction was applied. The whole array of stripes was divided into smaller elements, which can be visible in Figure 4.4. After that, the software calculated required dose factors, which change the base dose set for the whole structure, to compensate for the influence of adjacent elements. The structures with compensated doses visible as colors are shown in Figure 4.5. What can be seen is that the dose is compensated mostly at the edges of the whole arrays. In Figure 4.6 the optical microscope images of developed resist after exposition of quasiperiodic and periodic structures are shown. For structures exposition without proximity effect correction (a), contrast at the edges of the whole structures is visible, which can be connected to incompletely removed resist. This effect disappears after dose correction (b). The same observation can be made after material deposition and lift-off process, which is illustrated in Figure 4.7 showing the periodic structures. Figure 4.6 and show that the obtained stripes are not straight, which is an issue addressed in the next section.

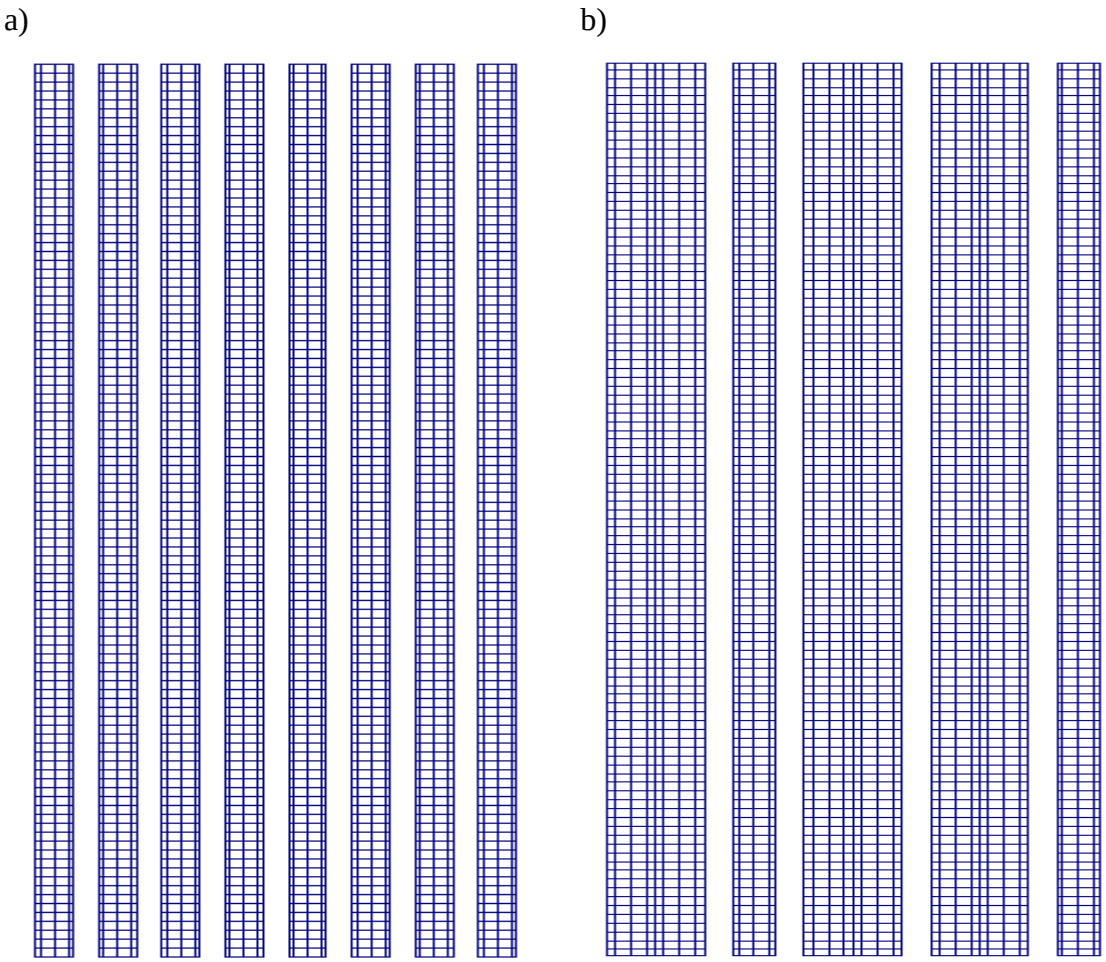

Figure 4.4 Part of periodic (a) and quasiperiodic (b) stripes array divided by software into smaller elements to compensate proximity effect.

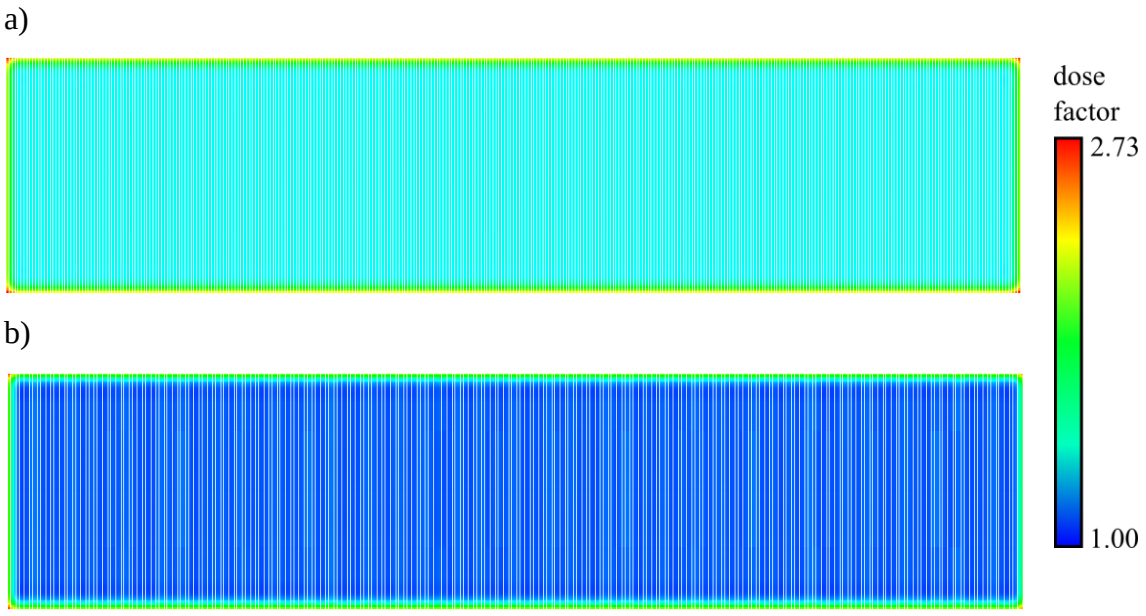

Figure 4.5 Map of corrected doses for periodic (a) and quasiperiodic (b) stripes array.

a) b)

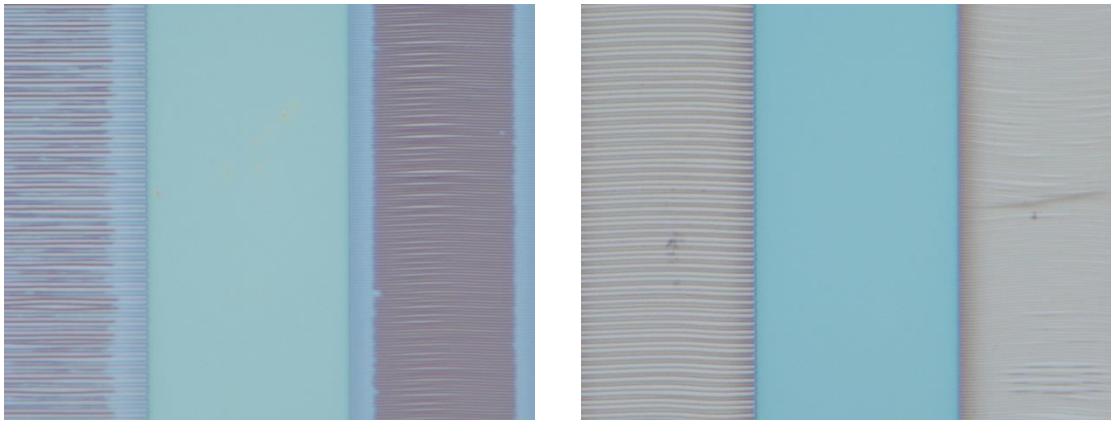

Figure 4.6 Images from optical microscope of developed resist after exposition with the same base dose of electrons of quasiperiodic and periodic structures without (a) and with (b) proximity effect correction.

a) b)

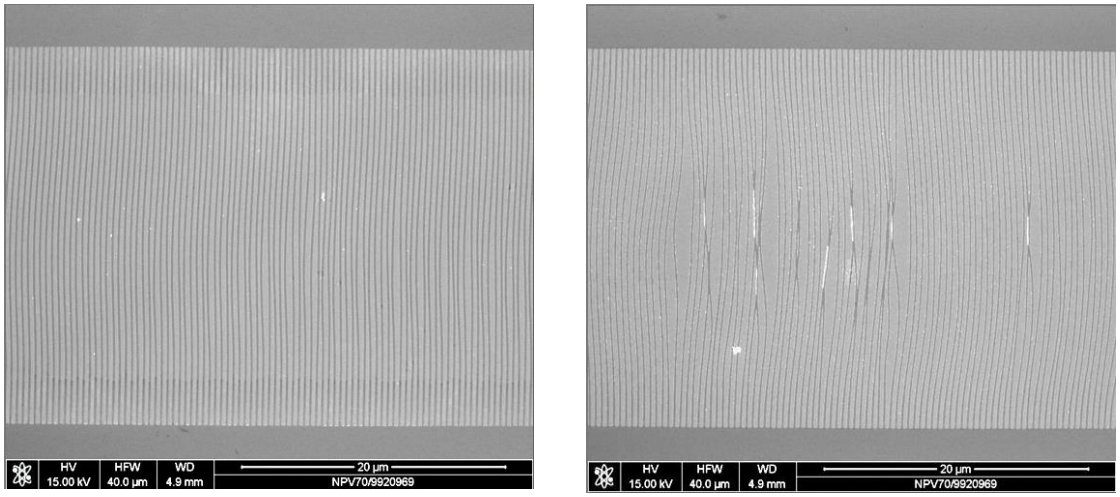

Figure 4.7 Images from SEM of periodic Py structures prepared without (a) and with (b) proximity effect correction.

4.1.3. Resist and electron dose selection

To obtain the array of straight stripes of dimensions close to the targeted, different resists configuration and electron doses were tested. In all of the structures, the voltage accelerating the electrons of 30 kV and beam current of about 100 pA were used. At the beginning, in the process of stripes array fabrication double layer of resist was used to prevent creation of the "garden fences" effect and to ease the lift-off process (see 2.3.1 and Figure 2.8). The first resist layer was MMA 8.5 2.5% deposited at the rotational speed of 6000 rpm for 60 seconds, so the thickness of obtained layer was ~68 nm. On the top of this layer PMMA 950K 1.5% was deposited at the 6000 rpm for 40 seconds to obtain the ~95 nm thick layer. The example of fabricated stripes is shown in Figure 4.8. The electron dose is given in the description under the figure

but one has to keep in mind that all of these numbers are base values, changed during the exposition process by the software proximity effect correction. The stripes are visibly deformed. Despite the fact that straight stripes were exposed, wavy structures were obtained, mostly bent in the middle of the stripes. The probable cause of this effect is that the bottom resist, which is more sensitive to the electrons, gets too narrow and does not stick to the substrate, because of the elements are packed so close to each other. It is more visible for the higher doses, which is shown in Figure 4.9. As an attempt to prevent this effect, an additional layer of adhesion promoter AR 300-80 was added before deposition of resist. This material, applied also by a spin coating process using a speed of 4000 rpm for 60 seconds and baked on a hot plate at 170 ^{o}C for 2 minutes makes approximately 15 nm thick layer which improves the strength of adhesion of the resist to the film deposited on it. Unfortunately, this solution failed to bring the expected improvement, which is visible in Figure 4.10. Another solution tested was to use more diluted bottom resist – MMA 8.5 1.5%. It was applied at 6000 rpm for 60 seconds so a thinner layer of ~39 nm was obtained. This could make the stripes of the bottom resist wider after the structures exposition and development and thus stick better to the substrate. An adhesion promoter was also used. The structures obtained with this resists configuration are shown in Figure 4.11. Unfortunately, this solution also failed to prevent the displacement of the stripes. In some cases, for lower electron dose it was possible to obtain straight stripes, although the quality of stripes edges was not satisfactory (shown in Figure 4.12).

a) b)

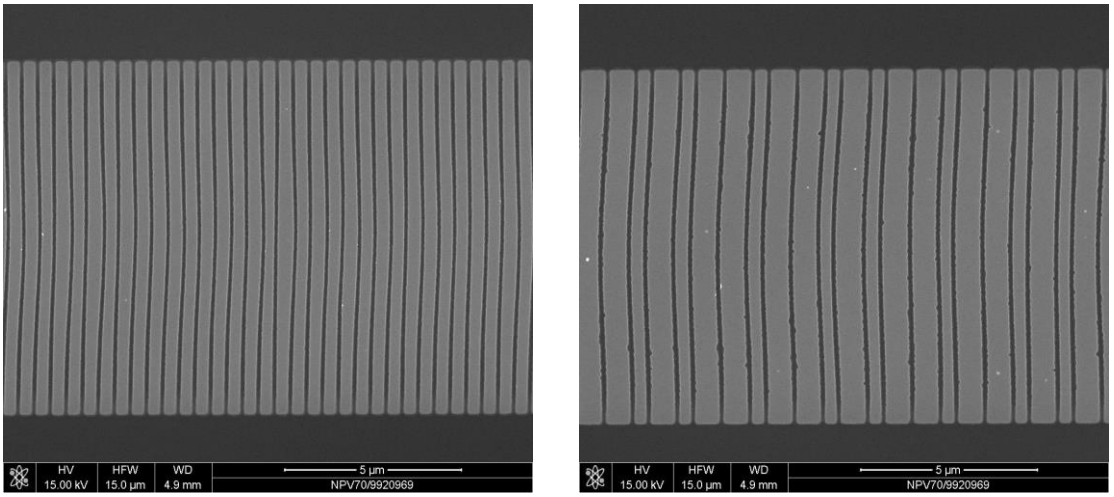

Figure 4.8 SEM images of periodic (base dose 257 µC/cm^2) (a) and quasiperiodic (base dose 199 µC/cm^2) (b) Py stripes arrays with visible deformations. Lithography process with: MMA 8.5 2.5% and PMMA 950K 1.5%.

a) b)

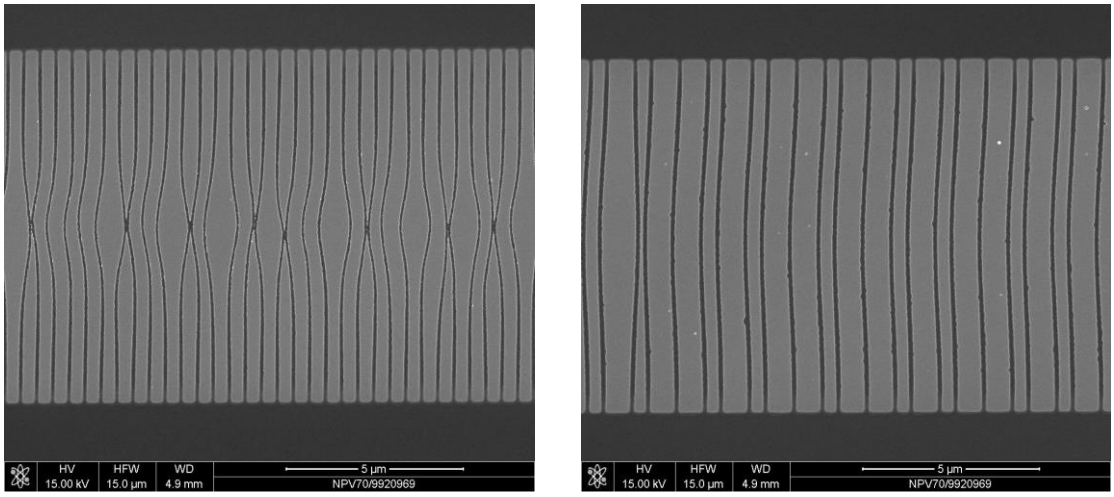

Figure 4.9 SEM images of periodic (base dose 293 µC/cm^2) (a) and quasiperiodic (base dose 222 µC/cm^2) (b) Py stripes arrays with visible deformations. Lithography process with: MMA 8.5 2.5% and PMMA 950K 1.5%.

a) b)

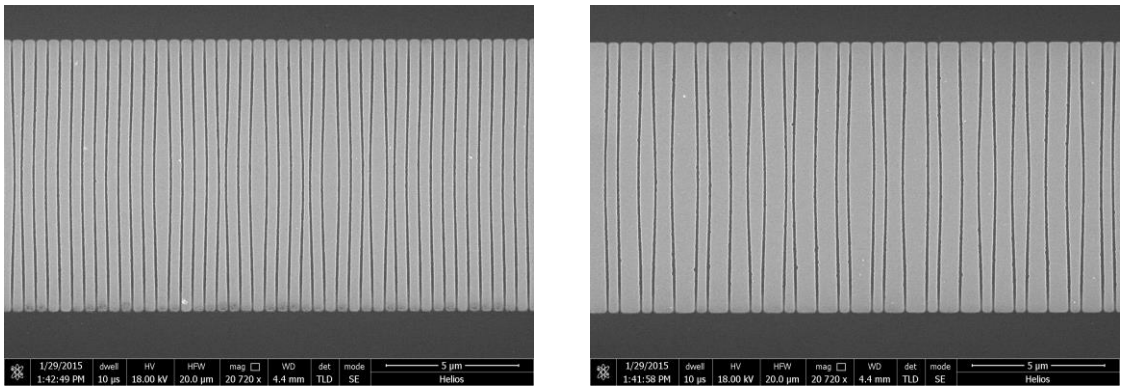

Figure 4.10 SEM images of periodic (a) and quasiperiodic (both base doses 187 µC/cm^2) (b) Py stripes arrays with visible deformations. Lithography process with: AR 300-80, MMA 8.5 2.5% and PMMA 950K 1.5%.

a) b)

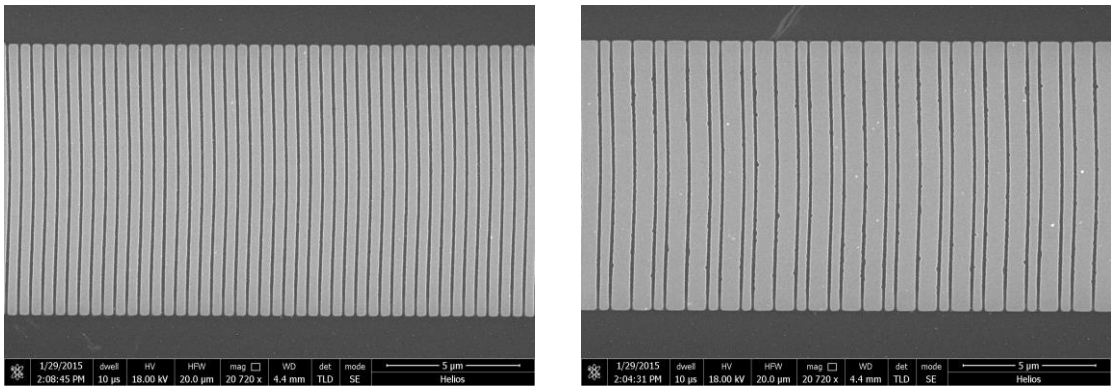

Figure 4.11 SEM images of periodic (a) and quasiperiodic (both base doses 176 µC/cm^2) (b) Py stripes arrays with visible deformations. Lithography process with: AR 300-80, MMA 8.5 1.5% and PMMA 950K 1.5%.

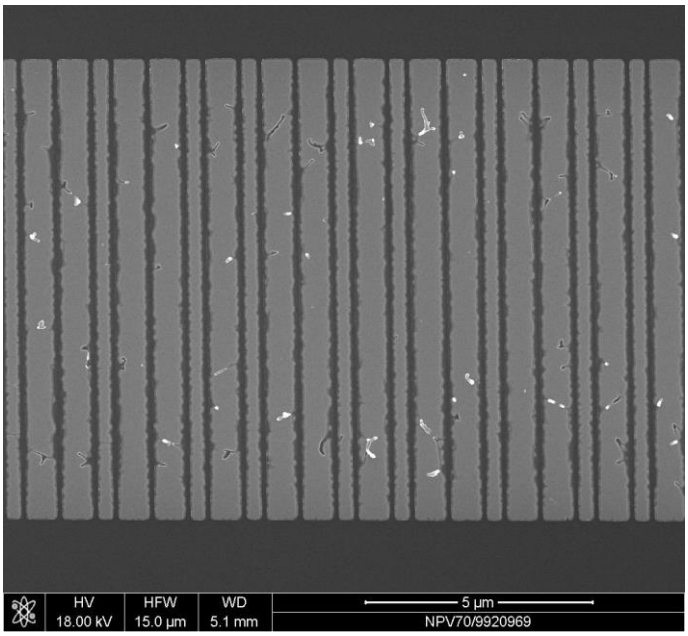

Figure 4.12 SEM images of quasiperiodic (base dose 164 µC/cm^2) Py stripes arrays with ragged edges. Lithography process with: AR 300-80, MMA 8.5 2.5% and PMMA 950K 1.5%.

Because using double resist layer during the electron-beam lithography process had led to fabrication of defected stripes array, for next tries only one resist was used: PMMA 950K 1.5% applied in spin coating process with 6000 rpm for 40 seconds. Although, as described in chapter 2.3.1, because of small undercut lift-off process was more difficult, in some structures, especially for lower doses, deposited material was not completely removed from the gaps. It is visible in Figure 4.13a as bright lines between the stripes. Another problem was that on SEM images, the stripes have much brighter edges in comparison with the ones fabricated using double layer of resist, which can indicate the "garden fences" effect (see Figure 2.6 and Figure 2.7), as shown in Figure 4.13b. Although overall it was possible to obtain straight stripes array of acceptable quality, for the fabrication of the samples used for magnetic properties measurements, only one resist was used.

a) b)

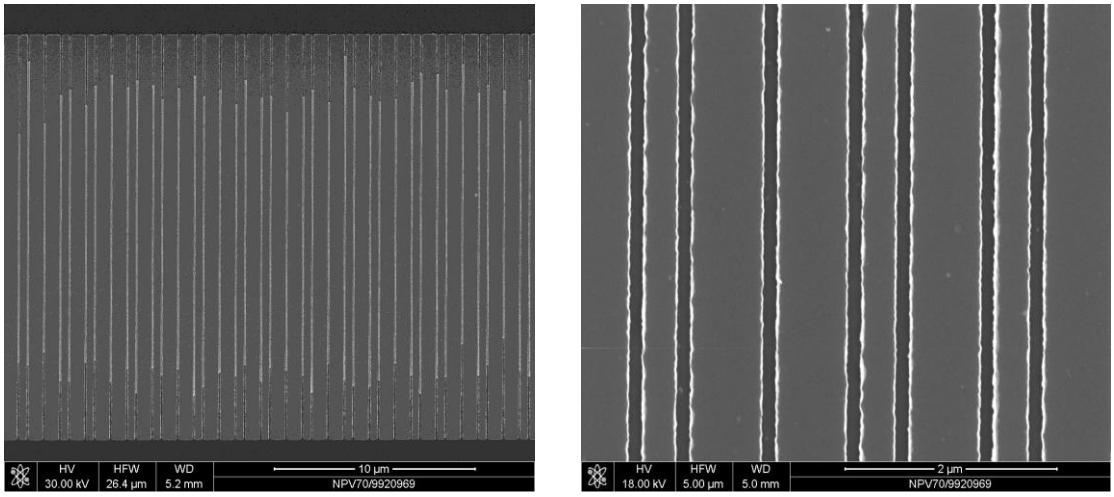

Figure 4.13 SEM images of quasiperiodic Py stripes arrays with visible not removed material from gaps between the stripe (a) and "garden fences" effect at the edges of the stripes (b). Lithography process with PMMA 950K 1.5%.

To optimize the electron dose needed for fabrication of stripes with desired dimensions (stripes of 350 nm and 700 nm wide), samples with different exposition doses used for structuring process were prepared. Additionally, to partially compensate for the fact that the dimensions of structures are greater for higher doses, the width of the stripes was reduced by 40 nm from each side. Figure 4.14 and Figure 4.15 show SEM images of respectively quasiperiodic and periodic structures for different base doses with measured width of the stripes. For quasiperiodic structures, the dose for which the width of the structures is closest to the desired is 152 $\mu C/cm^2$ and for periodic structures it is 164 $\mu C/cm^2$. Although it is important to note that these values can slightly differ for other samples, because no two samples are the same (for example the resist thickness can be different) and other parameters during the exposition like beam focus can also vary. Because of that, on each sample the structures are always exposed with a few different doses and the best one is chosen for further experiments.

a) 117 μC/cm^2 b) 129 μC/cm^2 c) 140 μC/cm^2

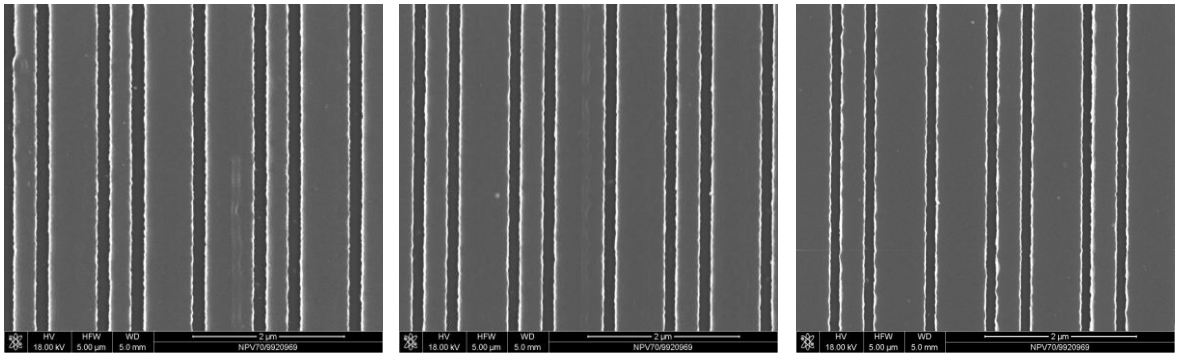

Narrow: 292±7 nm Narrow: 314±8 nm Narrow: 331±8 nm

Wide: 638±5 nm Wide: 656±12 nm Wide: 675±9 nm

d) 152 μC/cm^2 e) 164 μC/cm^2

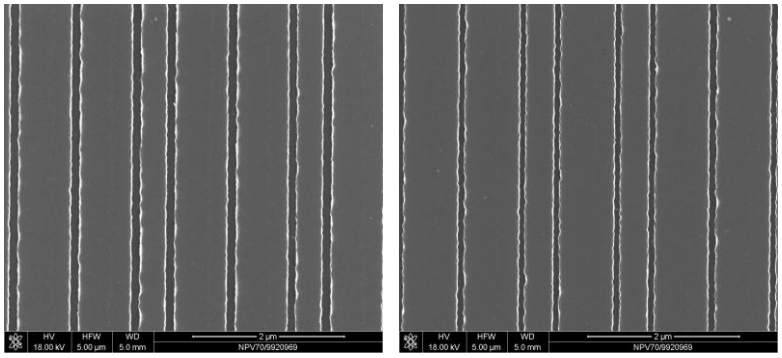

Narrow: 351±9 nm Narrow: 376±10 nm

Wide: 694±7 nm Wide: 723±13 nm

Figure 4.14 SEM images of quasiperiodic $Ni_{80}Fe_{20}$ stripes array for different base dose (above the images) of electrons and measured stripes width (under the images). Used resist: PMMA 950K 1.5%.

a) 117 μC/cm^2 b) 129 μC/cm^2 c) 140 μC/cm^2

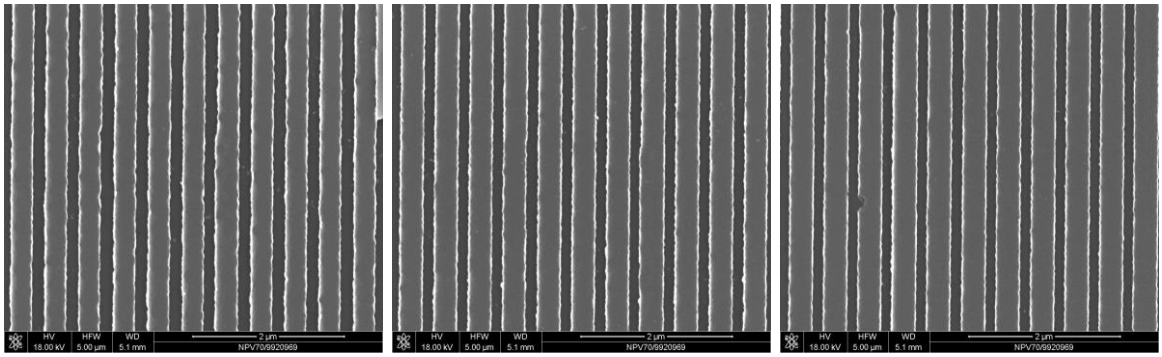

300±10 nm 316±6 nm 322±5 nm

d) 152 μC/cm^2 e) 164 μC/cm^2

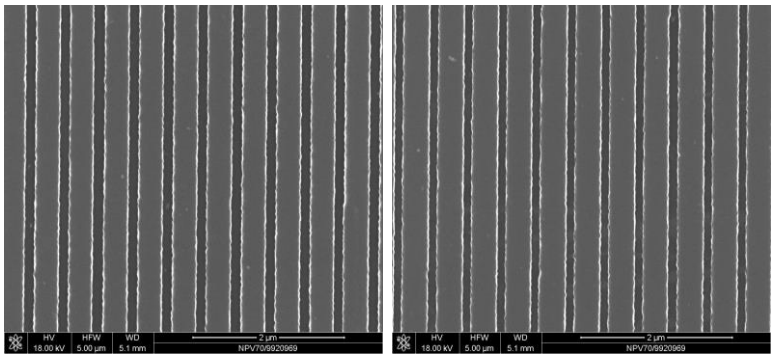

330±6 nm 351±6 nm

Figure 4.15 SEM images of periodic $Ni_{80}Fe_{20}$ stripes array for different base dose (above the images) of electrons and measured stripes width (under the images). Used resist: PMMA 950K 1.5%.

4.2. Optimization of coplanar waveguides fabrication by direct laser lithography

In this section optimization of fabrication of structures for spins excitation using direct laser lithography is described. It includes determination of resist thickness for different rotational speed during spin coating process, and selection of exposition dose.

4.2.1. Photoresist thickness

Just like in the case of electron-beam lithography, the first step to optimize the process of direct laser lithography was to measure the thickness of photoresist layer and select the right value. The emulsion used was positive photoresist 3540 diluted in 1:1 with AR 300-12. By using spin coater samples were coated at the rotational speeds: 2000, 3000, 4000, 5000 and 6000 rpm for 60 seconds each. Some simple structures were exposed and developed to obtain window which step could be measured with profilometer. The results of thickness for different substrate rotational speed are presented in Figure 4.16. The equation of the curve approximating this dependence is:

$$y = 600 * e^{-\frac{x}{2200}} + 390. \quad (4.4)$$

Because for this emulsion the lowest thickness possible to obtain was ~430 nm, a more diluted photoresist 3510 1:2 was used. For coating speed of 4000 rpm for 60 seconds the layer thickness is about 300 nm.

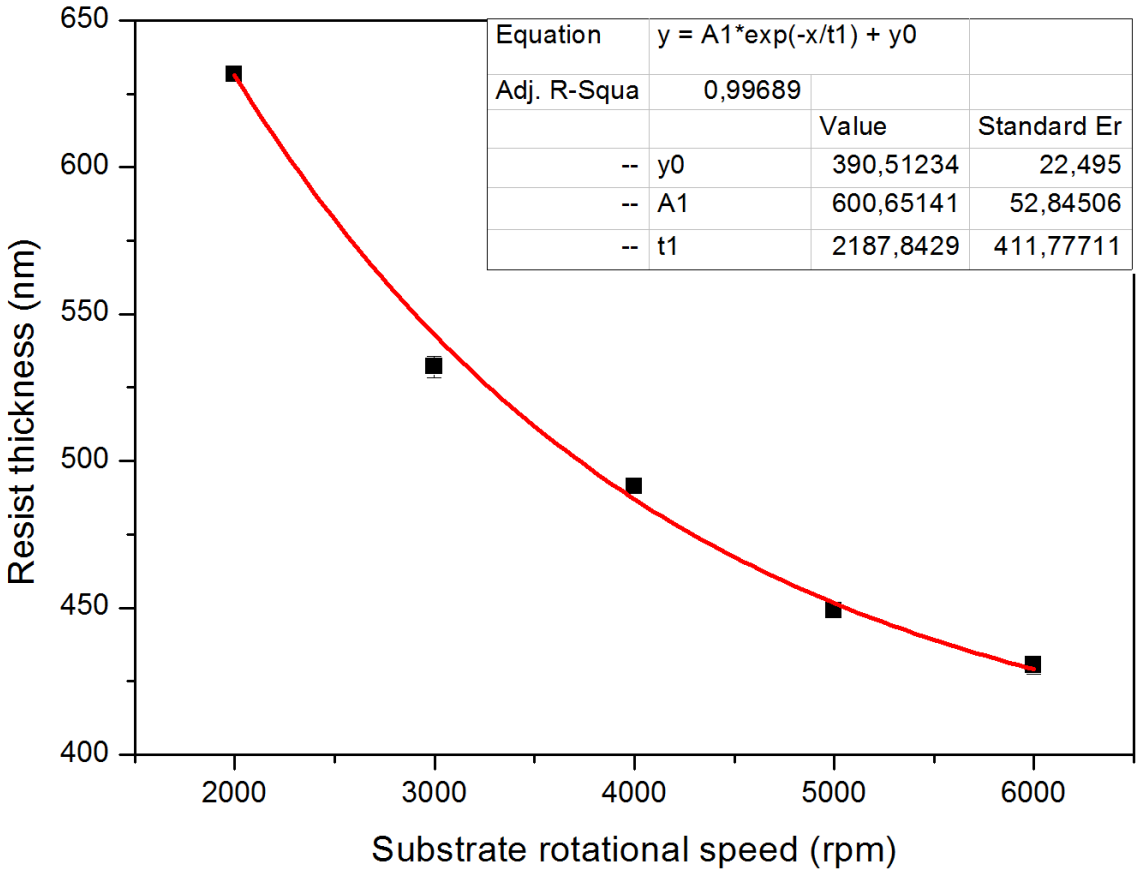

Figure 4.16 3540 1:1 photoresist thickness as a function of substrate rotational speed

4.2.2. Exposition dose selection

To select the right exposition dose for structures fabrication with given photoresist, sample with structures exposed with different doses was prepared. The photoresist layer was ~490 nm thick 3540 1:1 and tested doses: 10, 20, 25, 35 and 50 mJ/cm^2. After development, structures were imaged with optical microscope to check if all emulsion was removed. The obtained images are shown in Figure 4.17. For lower doses (10-25 mJ/cm^2) it is visible as colorful areas inside the exposed concentric lines that photoresist is not completely removed. For 35 mJ/cm^2 window in the photoresist up to the substrate is created, although edges are rough. For the highest dose of 50 mJ/cm^2 no photoresist is visible inside the exposed regions and this value was selected to fabricate structures. It is although important to realize that this kind of dose test has to be conducted every time the photoresist type of thickness is changed.

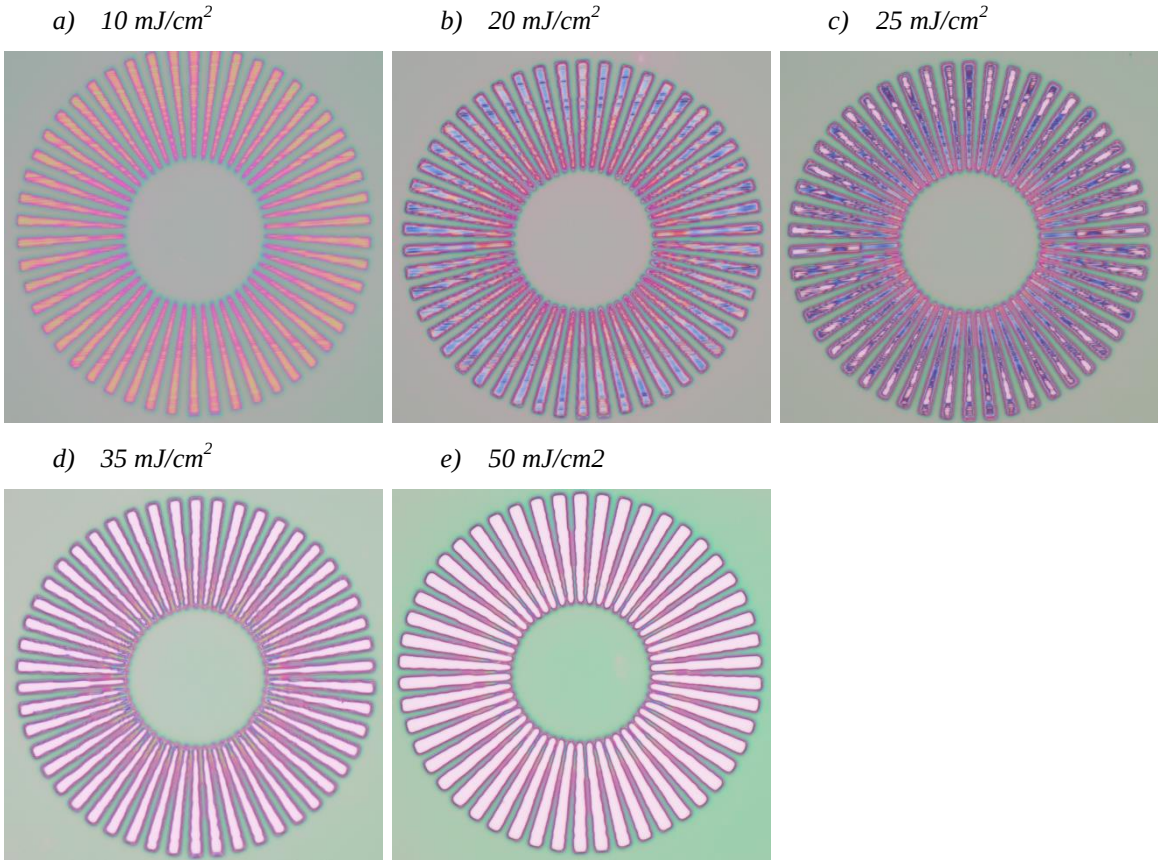

Figure 4.17 Optical microscope images after development of test structures for different exposition dose (above the images).

After dose optimization, coplanar waveguides used for ferromagnetic resonance and antennas for Brillouin light scattering measurements were fabricated. The structures are shown respectively in Figure 4.18 and Figure 4.19.

a) b)

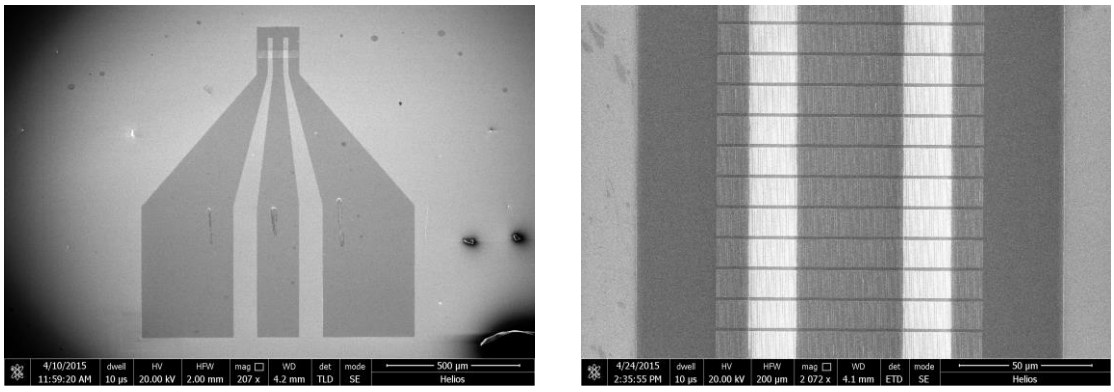

Figure 4.18 SEM image of coplanar waveguide for FMR measurements. The whole structure (a) and the close-up of signal and ground lines (b) with visible repeated stripes arrays as lighter rectangles. In (a) on the taper part visible are scratches from placing probes during the measurement.

a) b)

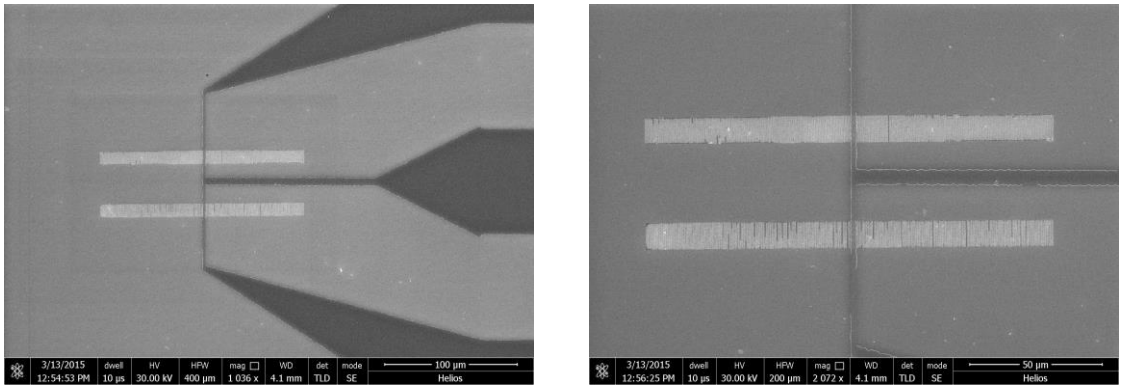

Figure 4.19 SEM image of structures for BLS measurements (seen as dark gray). The part of the structure (a) and the close-up of the lines (b) with visible stripes arrays as lighter rectangles.

5. MAGNETIC PROPERTIES OF MAGNONIC STRUCTURES CONSISTING OF STRIPES IN QUASIPERIODIC AND PERIODIC ARRANGEMENT

In this chapter results of static and dynamics magnetic properties of arrays consisting of Py stripes are presented. The structures were characterized with the following techniques: MOKE, MFM and VNA-FMR to determine their static and dynamics properties, respectively.

5.1. Static magnetic properties

To characterize the static magnetic properties of the structures, MOKE and MFM measurements were performed. The goal was to study magnetization reversal process in the individual stripes. Using magneto optical Kerr effect in longitudinal configuration (L-MOKE) hysteresis loops were determined from images of magnetic structure taken during magnetic field sweep. In Figure 5.1 the M-H major loop for quasiperiodic stripes array is shown (black line and dots). Field was applied along the grooves (easy axis of the Py stripes). Two magnetic fields corresponding to magnetization switch are observed: the first H_S^W occurring in the wider stripes ($45 \leq H_S^W \leq 100$ Oe), and the second H_S^N in narrower stripes ($145 \leq H_S^N \leq 185$ Oe). The type of stripes in which magnetization switches took place was assigned with the corresponding field ranges by observing the magnetic domain structure with MOKE and MFM techniques. The hysteresis loop was also measured with field applied perpendicular to the grooves. It is shown in Figure 5.2 and its shape is characteristic of magnetization reversal along the hard axis. The saturation field in this case is determined by the anisotropy field ($H_K \approx 300\ Oe$). The M-H major loop for periodic stripes array is shown in Figure 5.3 (black line and dots) for the field applied along and in Figure 5.4 for the field applied in perpendicular to the grooves. In M(H) graph in Figure 5.3 the point of inflection is visible which cannot be related to different width of stripes, because this structure consists of the stripes with the same width. Moreover, the field range in which this magnetization switch occurs is distinctly wider (from 75 to 175 Oe) as compared to H_S^N of the quasiperiodic structure. The two-step dependence observed for the periodic structure is probably caused by magnetostatic (dipolar) coupling of stripes, which favors antiferromagnetic configuration of magnetization directions in the stripes. This interpretation was confirmed by MFM measurements (see discussion concerning Table

5.4). In Figure 5.4 the shape of the loop also indicates harder axis although no saturation is visible. This indicates that the anisotropy field H_K of the narrow stripes is greater than the field used during the measurement.

Minor loops measurements were taken to check if there was any kind of interaction between stripes, which would prefer ferromagnetic or antiferromagnetic magnetization order. Samples were saturated in H = -300 Oe and L-MOKE signal was taken for the field changed to a specific maximum value after which it was decreased back to -300 Oe. Maximum values were chosen to be from the range between the saturation in one and the opposed direction. If the absolute value of the coercive field determined from the minor loop and related to reversal of the wide stripes H_C^W is smaller than the H_S^W determined from the major loop, the ferromagnetic interaction takes place between stripes. If this relation is the reverse ($H_C^W > H_S^W$), then antiferromagnetic interaction takes place. For the same values of these two fields, no interaction (or too weak to be sure) is observed. Another criterion is the displacement of the field value in the middle of hysteresis loop. Results for the quasiperiodic stripes structure are presented in Figure 5.1. For the minor loops there is no observed shift of H_C^W in relation to H_S^W, which could indicate no significant ferromagnetic or antiferromagnetic interaction between the wide and narrow stripes. However, the presence of some small magnetostatic interaction between these two kind of stripes can be determined from the fact that the narrow stripes in the quasiperiodic structure saturate in the slightly higher field (185 Oe) than in the periodic structure (175 Oe). It occurs because the wide stripes induce greater stray field and because of that the antiferromagnetic configuration between the narrow and the wide stripes is kept in a wider field range. In Figure 5.3 measurements for periodic stripes array are shown. For higher maximum values of applied field, some small shift of coercive field towards higher absolute values is visible. It is hard to establish if it is caused by the antiferromagnetic interaction between the stripes, although this kind of interaction, as mention before, can be determined by the inflection of the major loop.

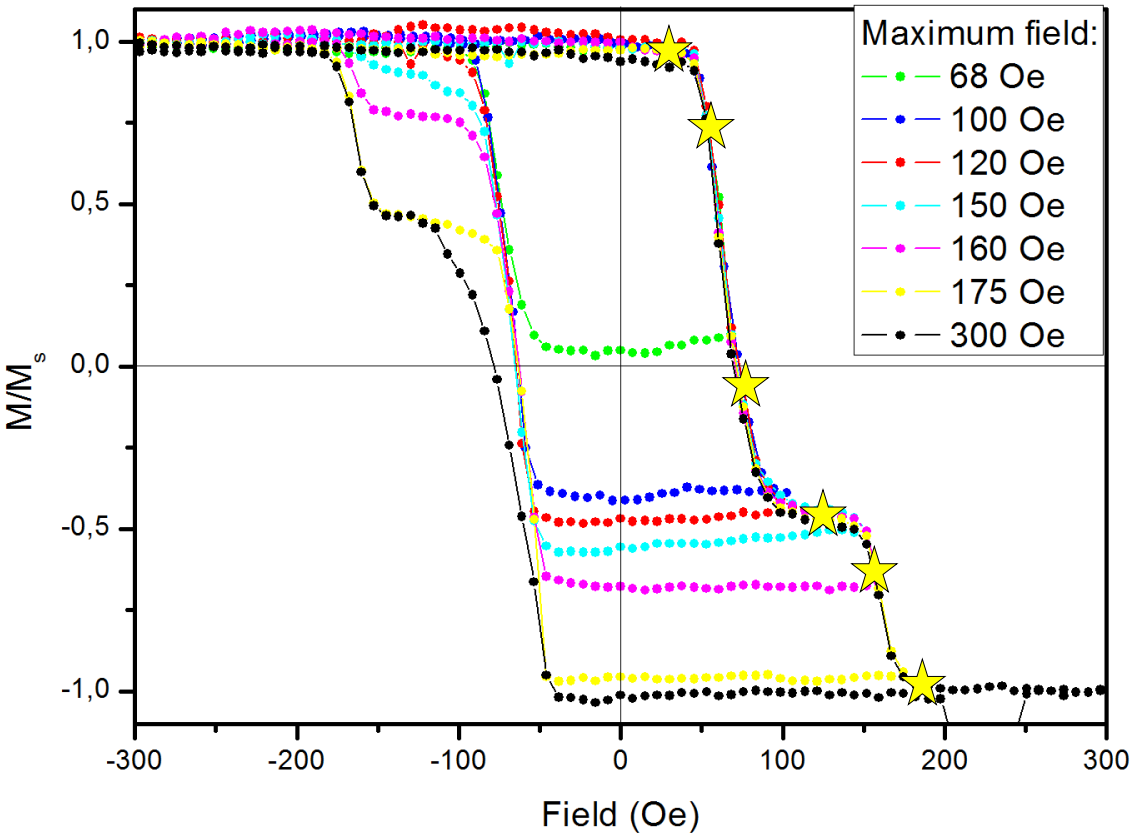

Figure 5.1 Normalized M-H loops of the quasiperiodic stripes array. Field was applied along the grooves. Stars indicate field values for which L-MOKE images were taken.

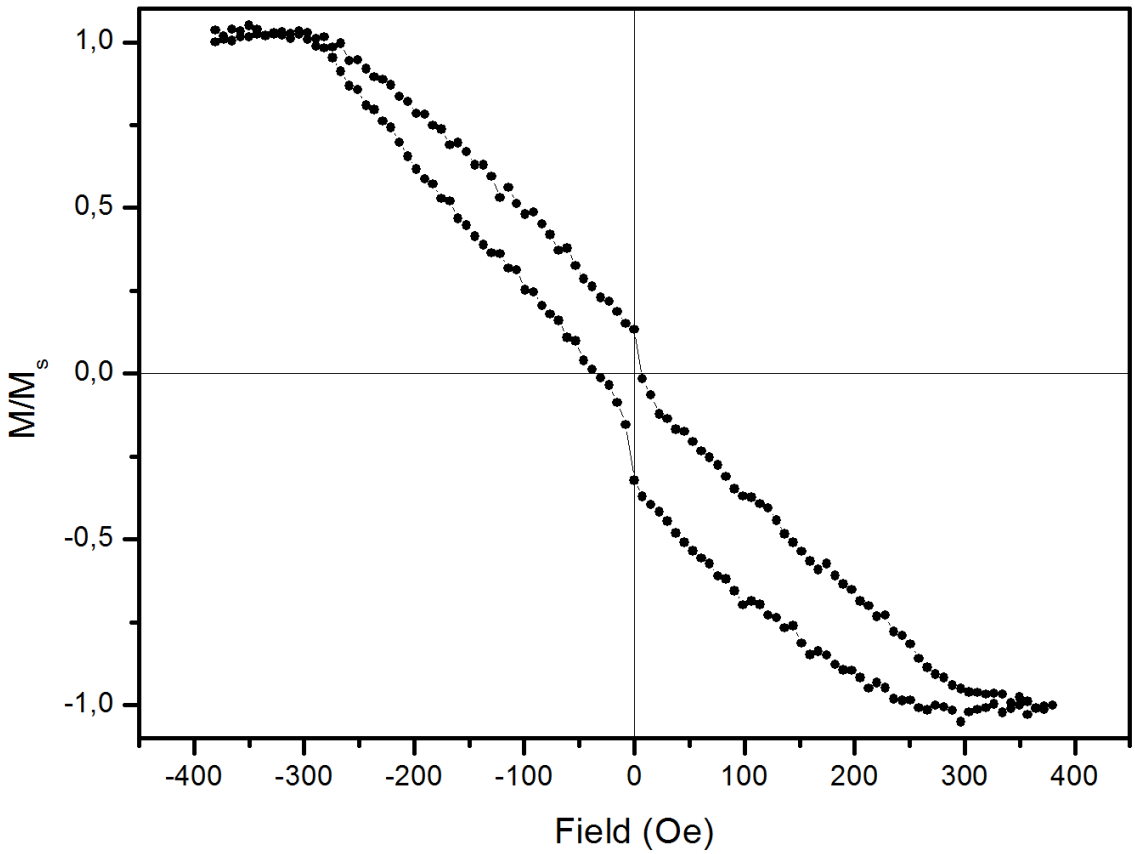

Figure 5.2 Normalized M-H loop of the quasiperiodic stripes array. Field was applied perpendicular to the grooves.

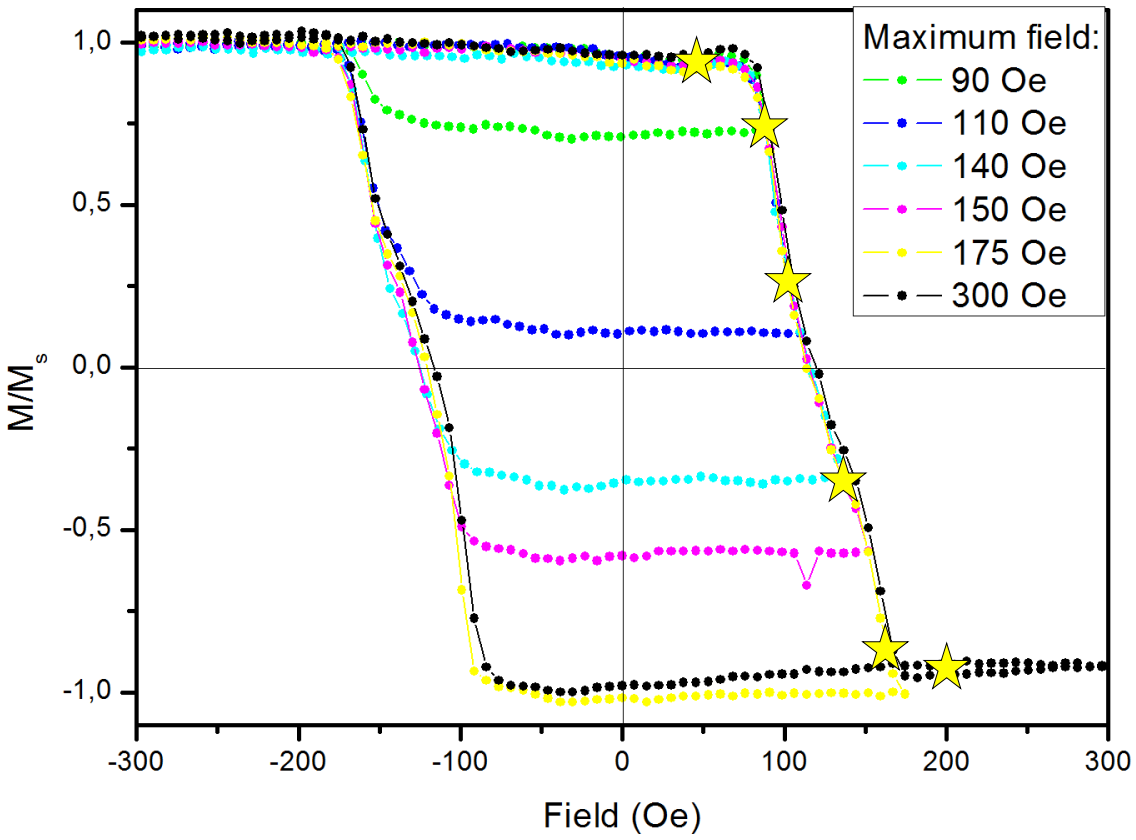

Figure 5.3 Normalized M-H loops of the periodic stripes array. Field was applied along the grooves. Stars indicate field values for which L-MOKE images were taken.

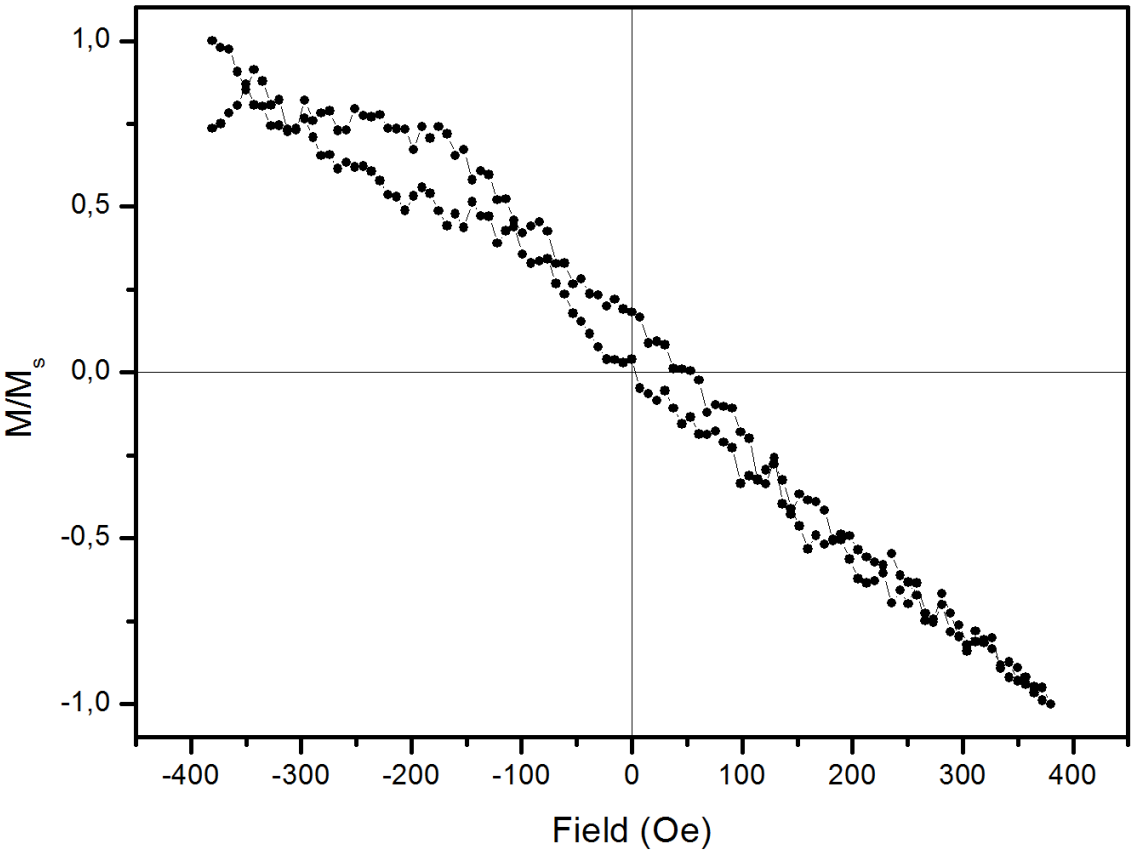

Figure 5.4 Normalized M-H loop of the periodic stripes array. Field was applied perpendicular to the grooves.

Using L-MOKE microscopy, changes in the magnetic structure with magnetic field were investigated. Samples were saturated in H = -300 Oe and then the magnetic field was changed towards 300 Oe with a step of about 10 Oe. In the images it is possible to see the contrast connected to the opposite magnetization directions in the stripes. Unfortunately, because of the limited resolution of the optical microscope used in this method, magnetization switching in single stripes, especially in the narrow ones, cannot be distinguished. Table 5.1 presents the representative images of the quasiperiodic stripes array in which a switch of the magnetization direction is observed upon sweeping of the magnetic field between -300 Oe and 300 Oe. Only about ~19 μm long part of the structure is visible as the light rectangles, between the signal and the ground CPW lines. At first, at H = 38 Oe a magnetization reversal of the wide stripes is observed. It is visible that the stripes change their magnetization direction randomly, in different parts of the structure. At H = 104 Oe the last wide stripe switches its magnetization. For $142 \leq H \leq 162$ Oe changes in the magnetic structure contrast are observed, connected with the magnetization switch in the narrow stripes. Table 5.2 presents the representative images for the periodic stripes array. The whole length of the structures is visible. The changes in the magnetic structure were observed for H range between 53 Oe and 197 Oe.

Table 5.1 MOKE images of magnetization direction switching in the quasiperiodic structure. The light rectangles are repeated structures in the gap between signal and ground CPW lines. Under each image field values for which it was taken are given. Magnetic field was applied along the grooves, as shown with the arrow in the first picture.

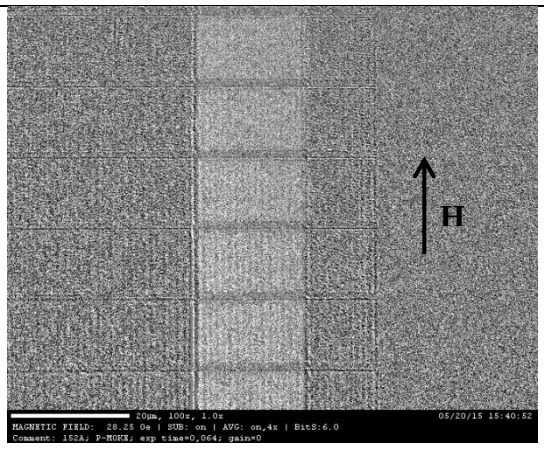	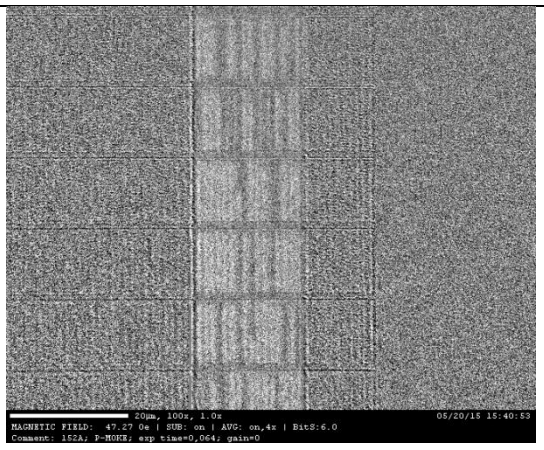
28 Oe	47 Oe

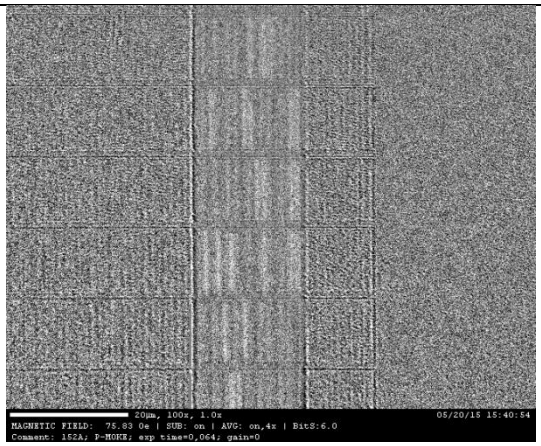	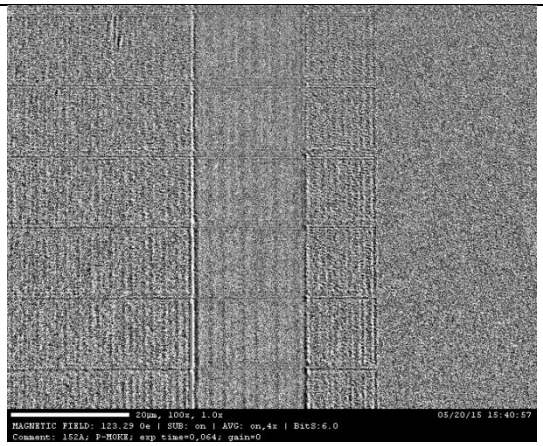
76 Oe	123 Oe
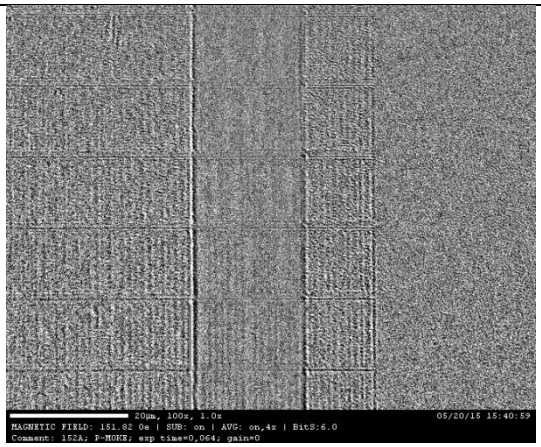	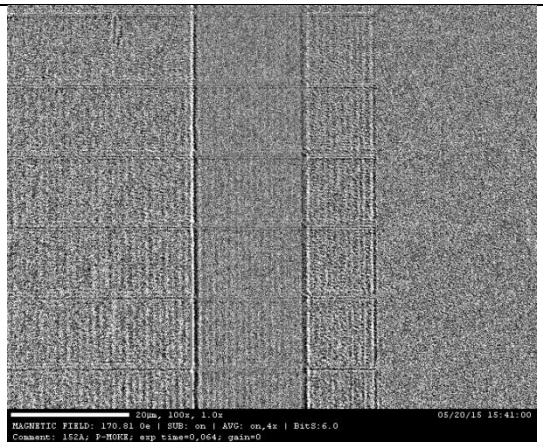
152 Oe	171 Oe

Table 5.2 MOKE images of magnetization direction switching in periodic structure. Repeated stripes arrays are visible. Under each image field values for which it was taken are given. Magnetic field was applied along the grooves, as shown with the arrow in the first picture.

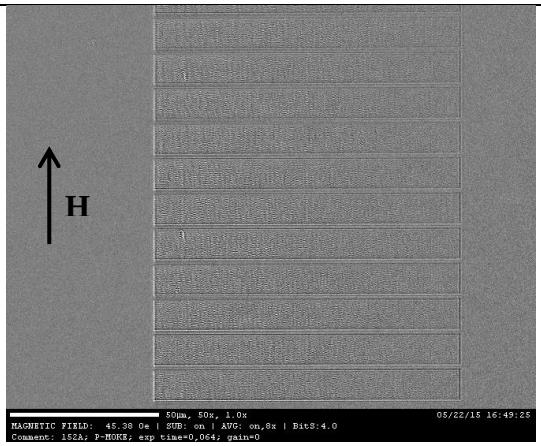	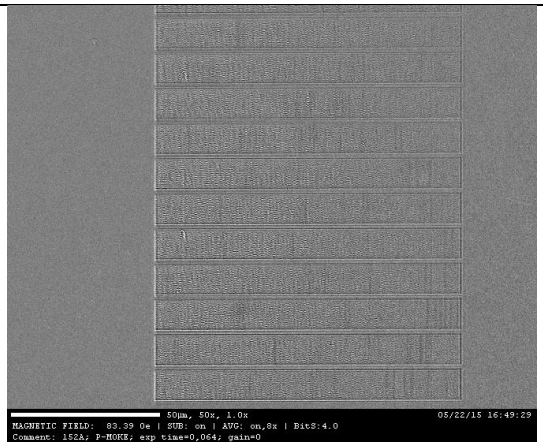
45 Oe	83 Oe

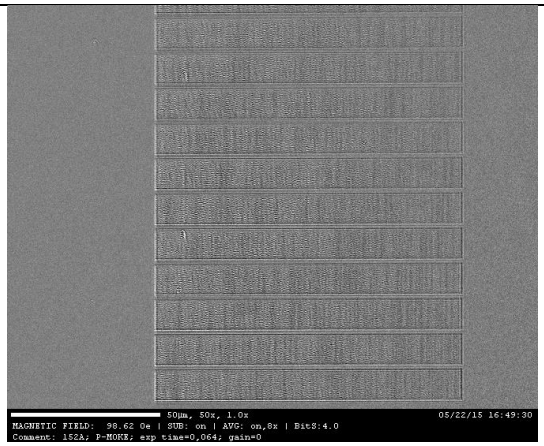

98 Oe

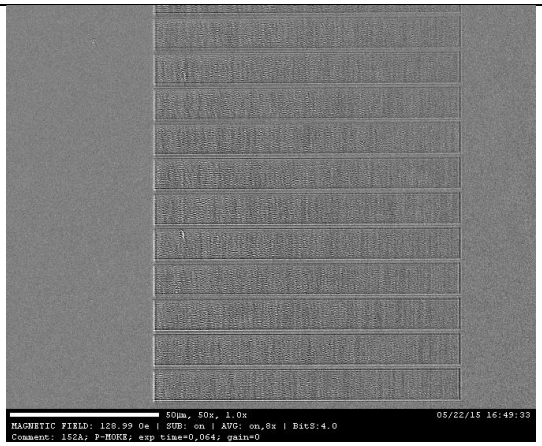

129 Oe

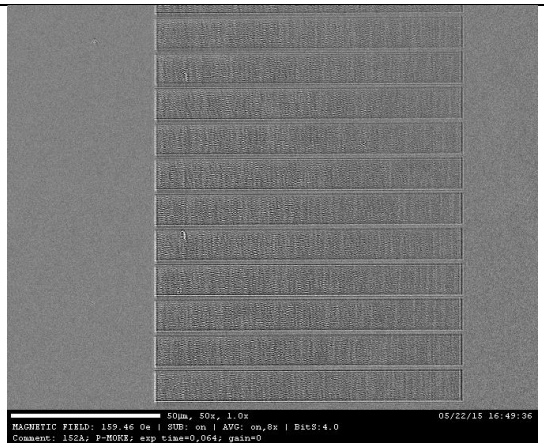

159 Oe

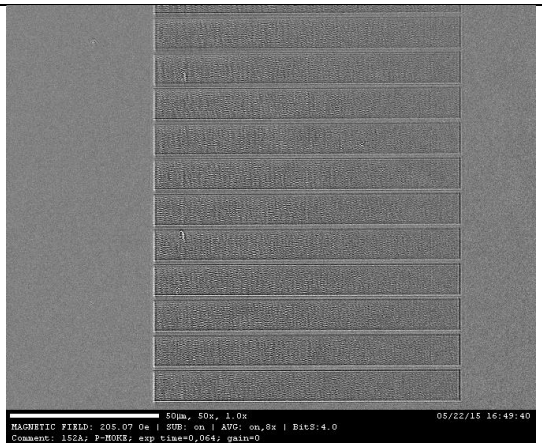

205 Oe

To observe magnetization switching in the single stripes, MFM measurements were performed and selected images are presented in Table 5.3 and Table 5.4 for the quasiperiodic and periodic stripes arrays, respectively. The first images in both tables are from the AFM scan which reveals the topography of the chosen area (12 x 12 μm^2) and shows the single narrow and wide stripes. All the next images are from MFM measurements of the same area and show the magnetic signal from the stray field at the ends of the stripes. It is possible to determine the relative direction of the magnetization in the stripes by looking at the colors of their ends. Single-domain state of the stripes is observed. Before measurements, the stripes were saturated by applying a field of $H = -300$ Oe along the grooves. Then the field was changed gradually to 300 Oe (and back to -300 Oe for quasiperiodic stripes array). For the quasiperiodic structures the first magnetization switch occurs at 50 Oe in the wide stripe. The magnetization switching in the wide stripes is observed up to 100 Oe, when all of them are magnetized in one direction (parallel to **H**), and all

narrow ones are magnetized in the opposite direction. As can be observed, when two wide stripes are adjacent to each other, the second one switches its magnetization in higher fields than most of the remaining wide stripes. This indicates some small antiferromagnetic interaction between the adjacent wide stripes. In the field from 170 to 190 Oe, the switching of magnetization in the narrow stripes is visible. For periodic structures, the magnetization switching is observed between 100 and 220 Oe. The antiferromagnetic order of stripes in the large parts of the scanned structure is observed as alternating light and dark dots at the ends of the stripes in the field range corresponding to the inflection of the hysteresis loop from Figure 5.3. This confirms the antiferromagnetic interaction between the narrow stripes as indicated by the inflection in the hysteresis loops measurements.

Table 5.3 AFM/MFM images of quasiperiodic stripes structure. Under each image field values for which it was scanned are given. Magnetic field was applied along the grooves. The first is AFM image of topography. The others are MFM images which show magnetic contrast at the ends of the stripes. Scanned area: 12 x 12 μm^2.

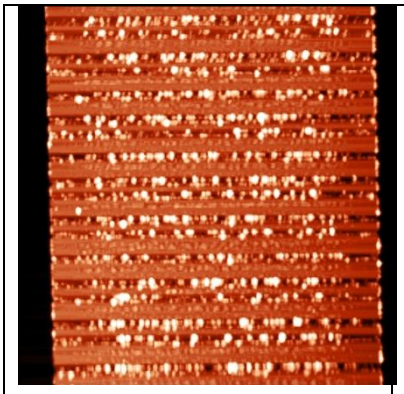	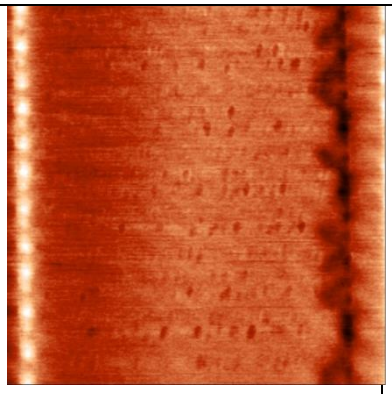	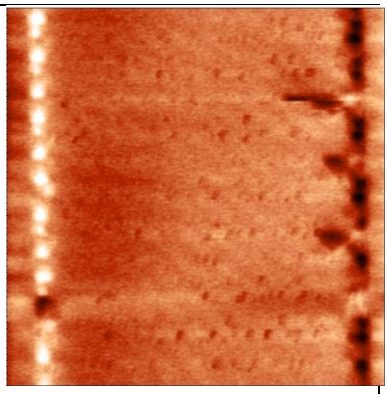
AFM image	Sat. in -300 Oe, 0 Oe	+50 Oe
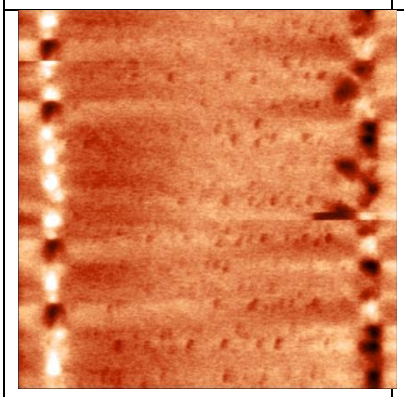	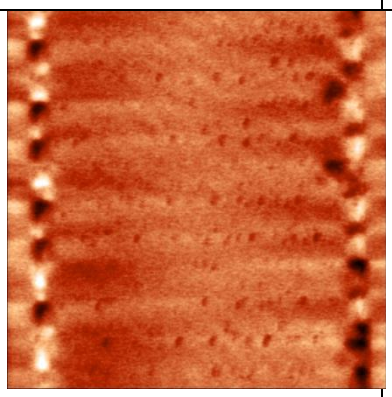	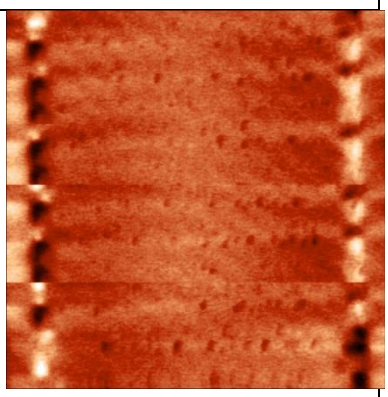
+60 Oe	+70 Oe	+80 Oe

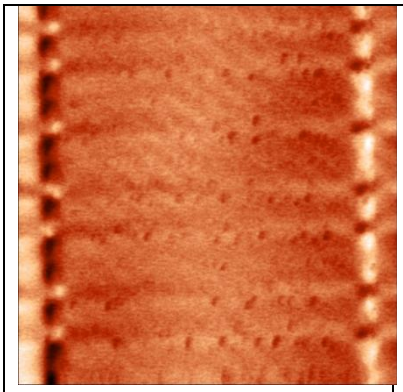

+100 Oe

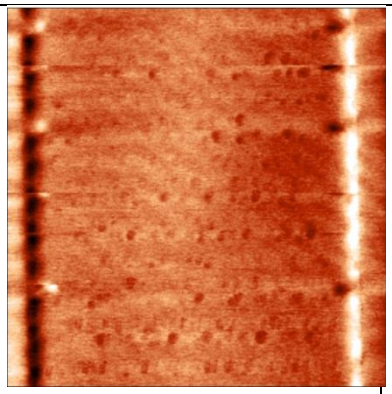

+180 Oe

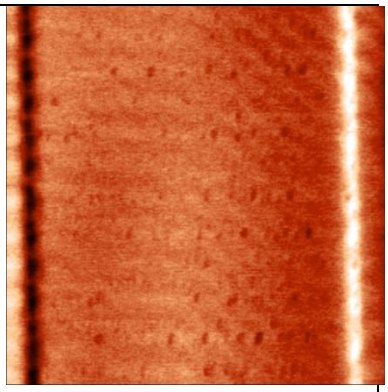

+190 Oe

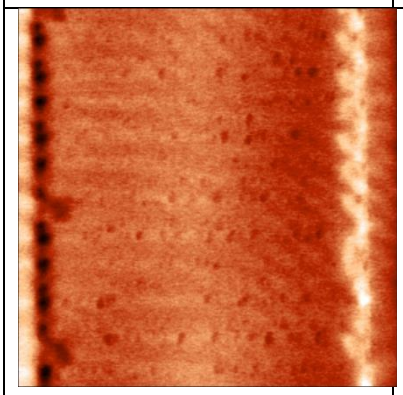

Sat. in +300 Oe, 0 Oe

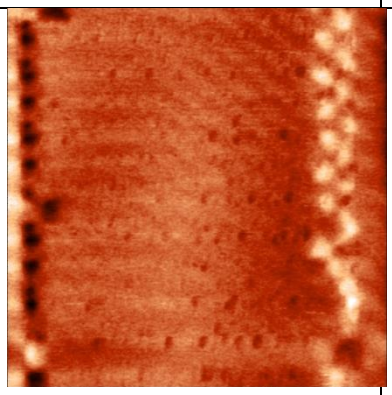

-60 Oe

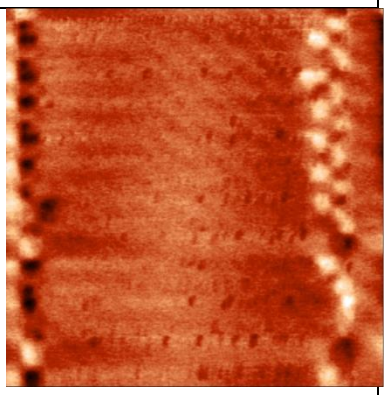

-70 Oe

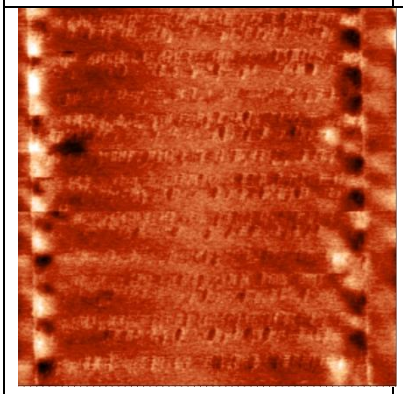

-80 Oe

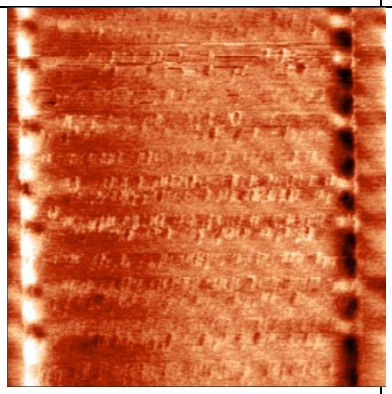

-100 Oe

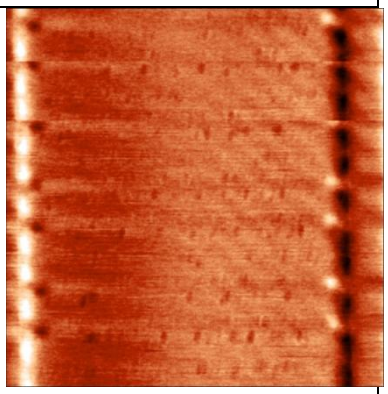

-190 Oe

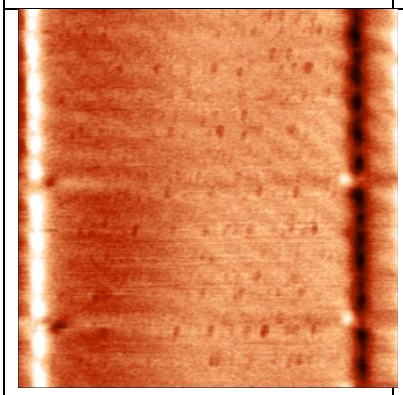

-200 Oe

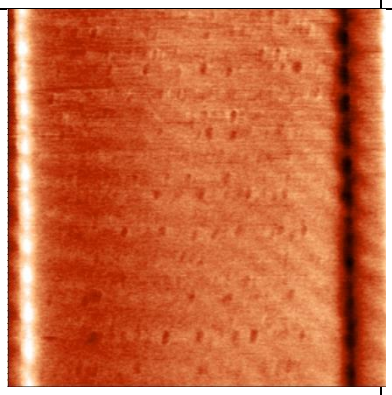

-210 Oe

Table 5.4 AFM/MFM images of periodic stripes structure. Under each image field values for which it was scanned are given. Magnetic field was applied along the grooves. The first is AFM image of topography. The others are MFM images which show magnetic contrast at the ends of the stripes. Scanned area: 12 x 12 μm^2.

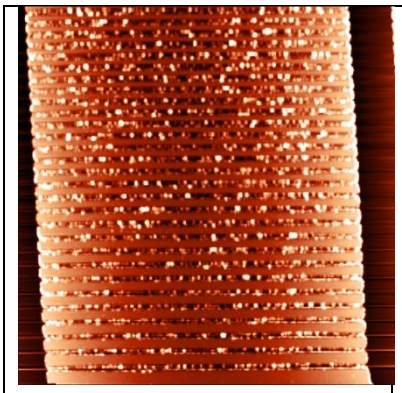	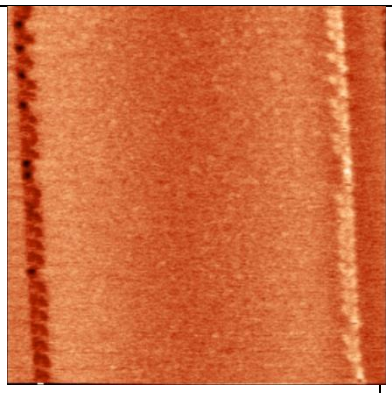	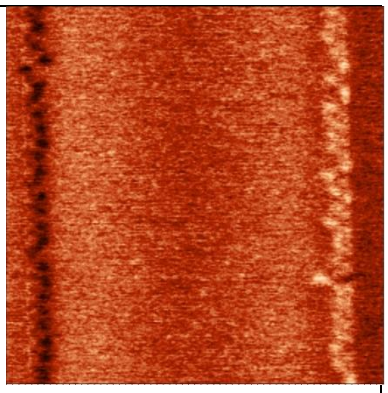
AFM image	Sat. in -300 Oe, 0 Oe	+100 Oe
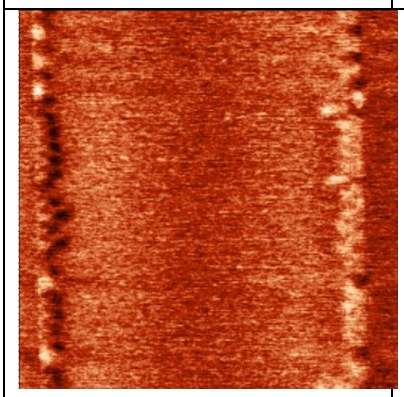	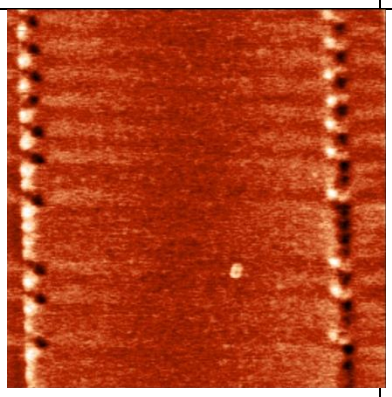	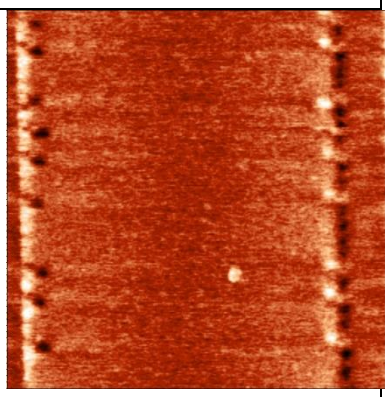
+120 Oe	+150 Oe	+180 Oe
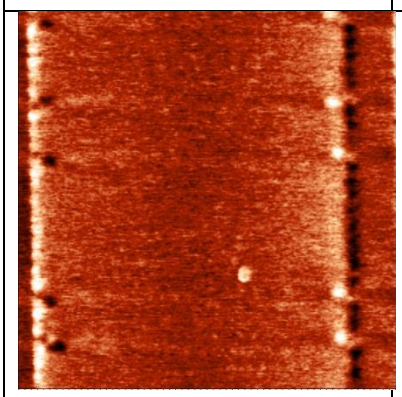	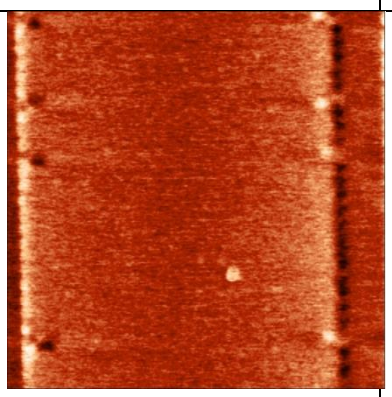	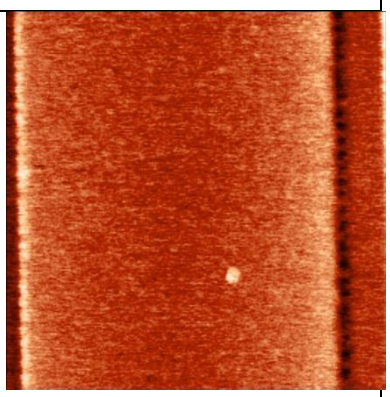
+190 Oe	+200 Oe	+220 Oe

5.2. Dynamic magnetic properties

Ferromagnetic resonance was measured using vector network analyzer and coplanar waveguides integrated with the samples. To enhance the signal, arrays of stripes were repeated along the CPW signal line 13 times with distance between adjacent ones about 1.5 μm. Part of this structure can be seen in Figure 4.18 b). The magnetic field was applied along the grooves and changed in steps of about 10 Oe from -440 Oe to 440 Oe

(forward half of the hysteresis loop). For each value of magnetic field, measurement of ΔS_{22} for the set frequency range was taken and after that all the plots were collected and presented as one graph of frequency vs. magnetic field, where ΔS_{22} signal was shown in a color scale. As described in chapter 2.5.2, a reference technique was used to improve the signal-to-noise ratio. Because of the setup limitations, field could only be applied in one direction with the maximum value of about 550 Oe, for which the resonance frequency was still observed in the measured frequency range. Because of that, on some of the graphs reference peaks are visible as straight horizontal red lines. In some cases it was possible to take the reference signal in the external field perpendicular to the grooves which was applied manually with magnets. As a result, these horizontal lines from reference measurement were not visible.

Data from VNA-FMR measurement for quasiperiodic stripes array are presented in Figure 5.5. One strong mode starting at frequency of 8 GHz at -440 Oe and additional, very weak two modes (10.5 GHz and 12.5 GHz at -440 Oe) can be observed. The main absorption peak is collective (acoustic) mode, which is assigned to the spatially uniform magnetic field around the CPW. It is characterized by the in-phase magnetization precession in adjacent stripes [1]. In this mode, the resonance frequency decreases while the field changes its value from -440 to 55 Oe. Then the frequency shift is observed towards higher frequencies and the resonance frequency of this mode starts to increase with magnetic field up to about 150 Oe at which the second shift is visible and after that continued growth. The second mode, as evidenced by the initial micromagnetic simulations [24] is the optical in which magnetizations in narrow and wide stripes are in the opposite phases and the observed signal comes mainly from the narrow stripes. The dependence of this mode on frequency is similar to that of the main mode, although between 55 and 150 Oe, when the strongest mode starts to increase, the second is still decreasing. The third mode is too weak to accurately describe its behavior. The field values at which frequency jumps are observed are in good agreement with the values at which magnetization reversal in the stripes takes place (see Figure 5.1). As shown in the previous chapter, the first reversal at 55 Oe occurs in the wide stripes and the second at 150 Oe in the narrow ones. So in the field range from 55 to 150 Oe, magnetizations in the narrow and the wide stripes are in antiparallel order and in the rest – parallel. The results obtained for the main mode for the quasiperiodic structure are

qualitatively similar to those reported in Ref. [1] for the periodic structure of stripes with alternating width 200 and 540 nm.

For the periodic structure for which the data are presented in Figure 5.6, only one strong absorption peak is observed from collective excitation of the magnonic crystal [9], which starts at 9.5 GHz for -440 Oe and decreases down to the field of 80 Oe. Then resonance frequency starts to increase (the signal observed in this region is weaker) and at 180 Oe it switches towards higher frequencies and continues to increase. Here also, when comparing with the hysteresis loop (Figure 5.3) the field range from 80 to 180 Oe is in good agreement with the range in which the magnetization direction switch takes place in the stripes.

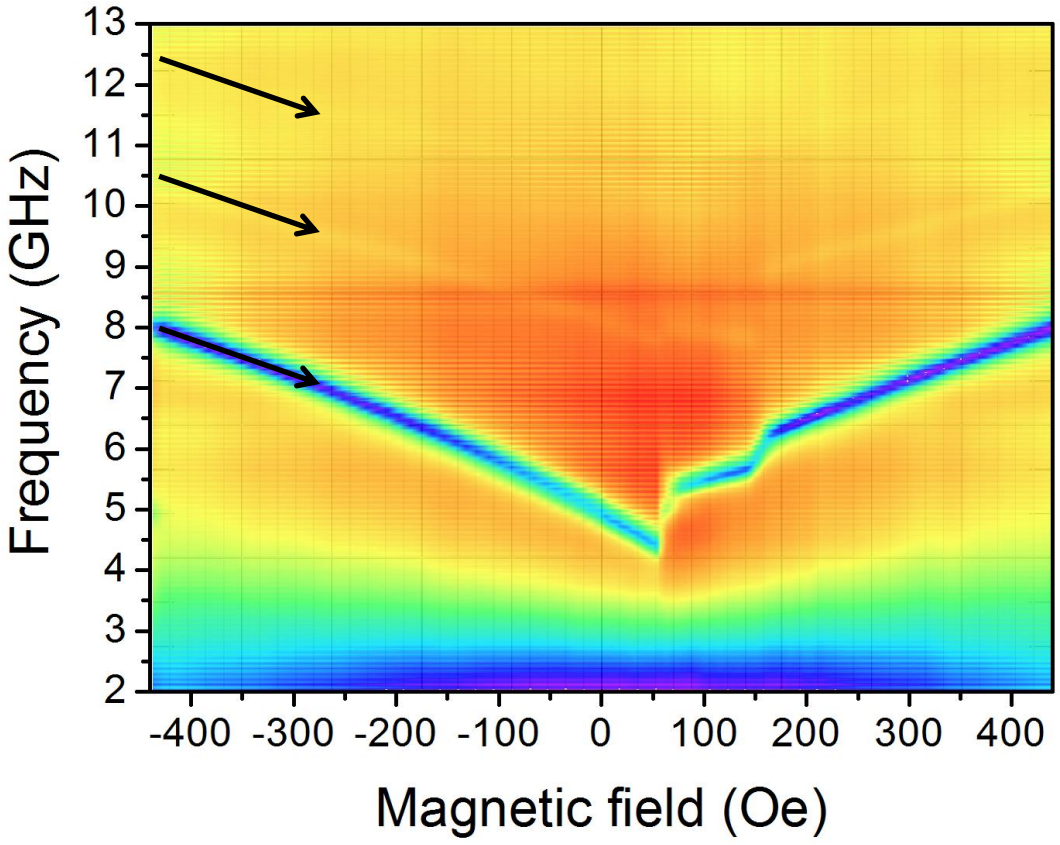

Figure 5.5 ΔS_{22} signal as a function of magnetic field for quasiperiodic stripes array. The arrows indicate lines of resonance absorption - spin excitations.

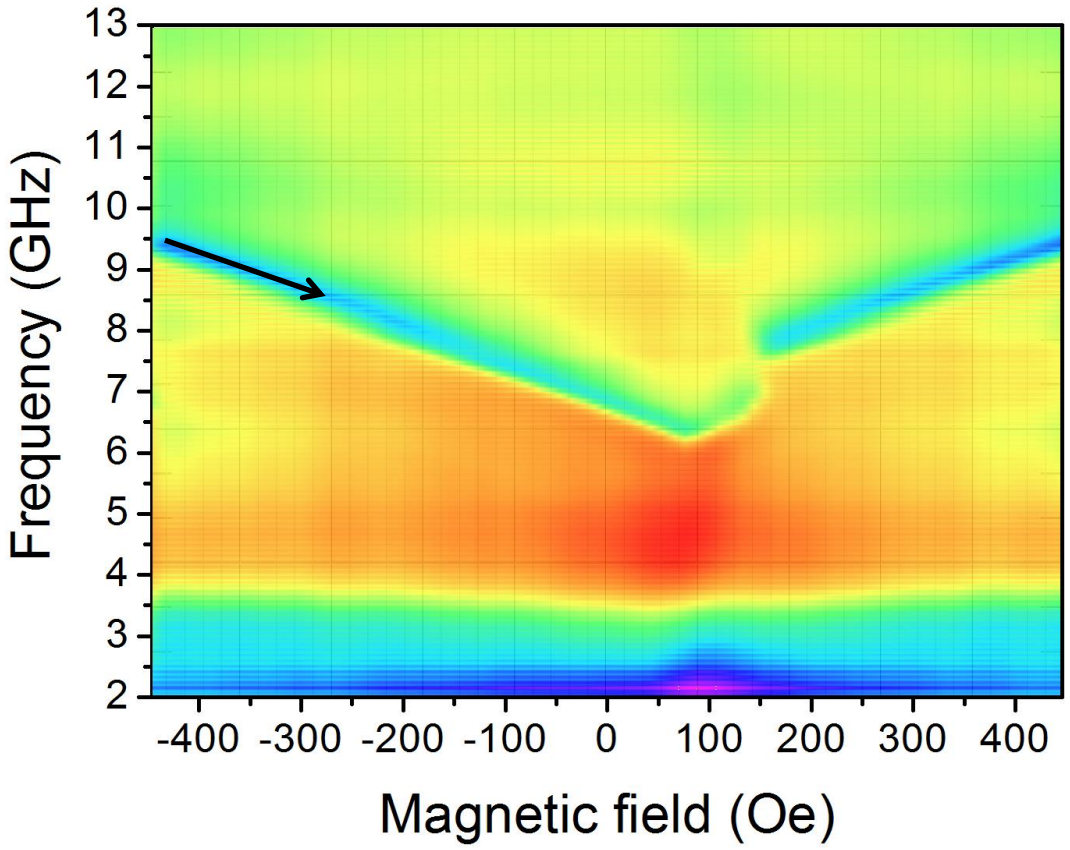

Figure 5.6 ΔS_{22} signal as a function of magnetic field for periodic stripes array. The arrow indicates the line of resonance absorption.

The VNA-FMR measurements in the backward halves of the minor loops were taken. At first, sample was saturated along the stripes in H = 550 Oe and then the magnetic field was slowly decreased to the chosen minimum field negative value H_{min}. From that, measurement was started with field changing again in direction of positive values. Figure 5.7 presents the results for quasiperiodic structures. As for minor loops measurements, the minimum field was chosen to be from the range in which magnetization is in the process of switching (after the first and before the last full frequency jump). For quasiperiodic structures, three selected minimum field values were: (a) -147 Oe (middle of the second frequency shift), (b) -99 Oe (between two frequency shifts) and (c) -67 Oe (middle of the first frequency shift). For (a) all of wide and part of narrow stripes should switch its magnetization (see Table 5.3 for 180 Oe). That is why the frequency shift, connected with wide stripes, is visible around 55 Oe. The frequency jump is preceded by a small increase in the mode frequency, which is not observed in Figure 5.5. At 150 Oe slight a frequency jump is also visible, associated with magnetization switch in remaining narrow stripes. From this field value, a stronger signal is observed. For (b) and (c) only one frequency shift, connected with wide stripes

is observed. In (b) wide and narrow stripes are in antiparallel order (Table 5.3 for 100 Oe), and in (c) some of the wide stripes should be in their initial state (Table 5.3 for 70 Oe) Here also range in which frequency of the mode is increasing before switching to higher values is observed. As for the second mode, unfortunately it is only visible in the image (a). Its frequency dependence is similar to that from Figure 5.5 except for the range from the minimum field to about 0 Oe. Additional nonmonotonic branch is visible, connected to antiferromagnetic order in stripes [9], which starts in the field of -149 Oe at 7.8 GHz. Then these two branches merge.

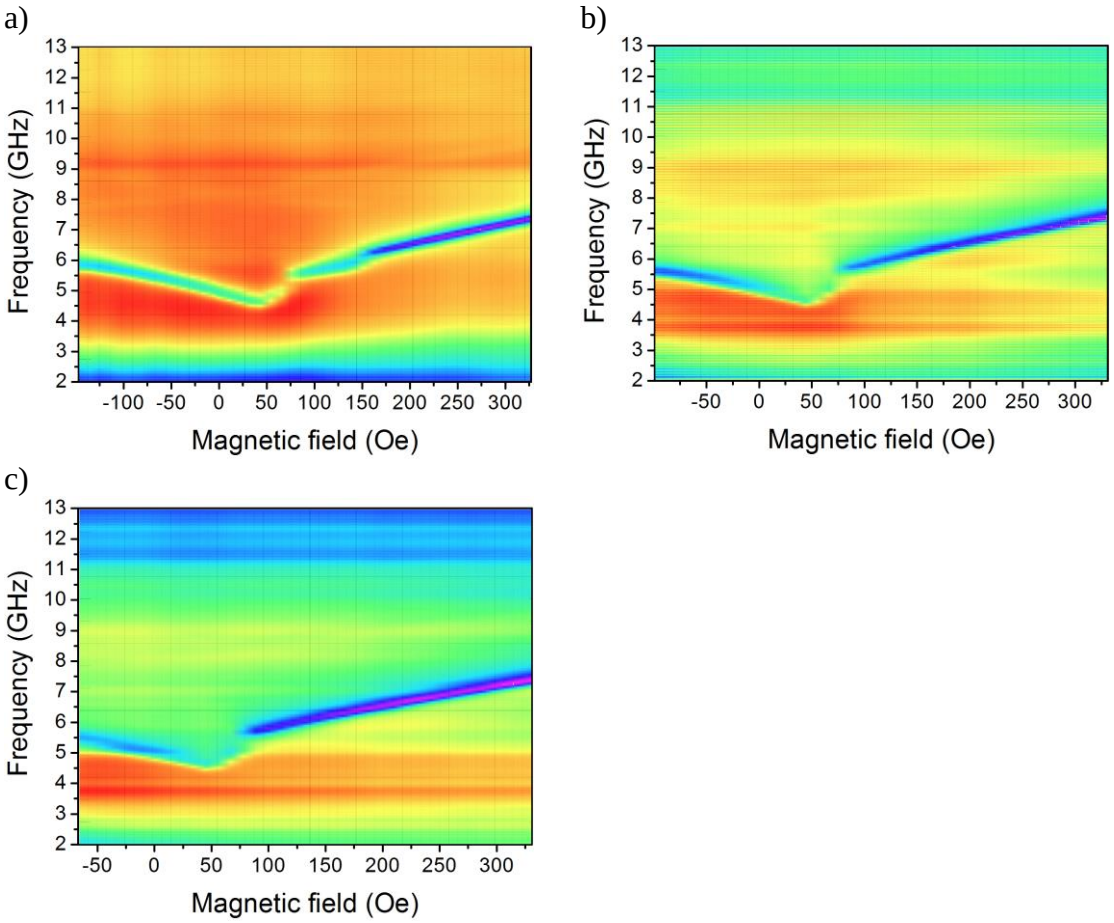

Figure 5.7 FMR absorption spectra in the minor loops with H_{min} = -147 Oe (a), -99 Oe (b) and -67 Oe (c) for quasiperiodic stripes array.

For periodic stripes structures, the results for the backward half of minor loop VNA-FMR measurements are presented in Figure 5.8. In all these graphs except for (b) horizontal red reference lines at 10 and 6.8 GHz are visible. For (a) the minimum field was chosen to be after the magnetization switch (almost clear ferromagnetic order, see MFM image in Table 5.4 for 180 Oe), so a dependence similar to that for full field range is visible. For (e) we observe monotonically rising branch connected to the ferromagnetic order of the stripes (minimum magnetic field is before the switch,

see Table 5.4 for 100 Oe). In (c) and (d) a nonmonotonic curve is observed, connected with antiferromagnetic state of the magnetization in the stripes (Table 5.4 for 150 Oe) [9]. For (b) two branches are visible: one nonmonotonic and the other decreasing from 8.1 GHz at -144 Oe, which looks like a transition between the ferromagnetic and antiferromagnetic order.

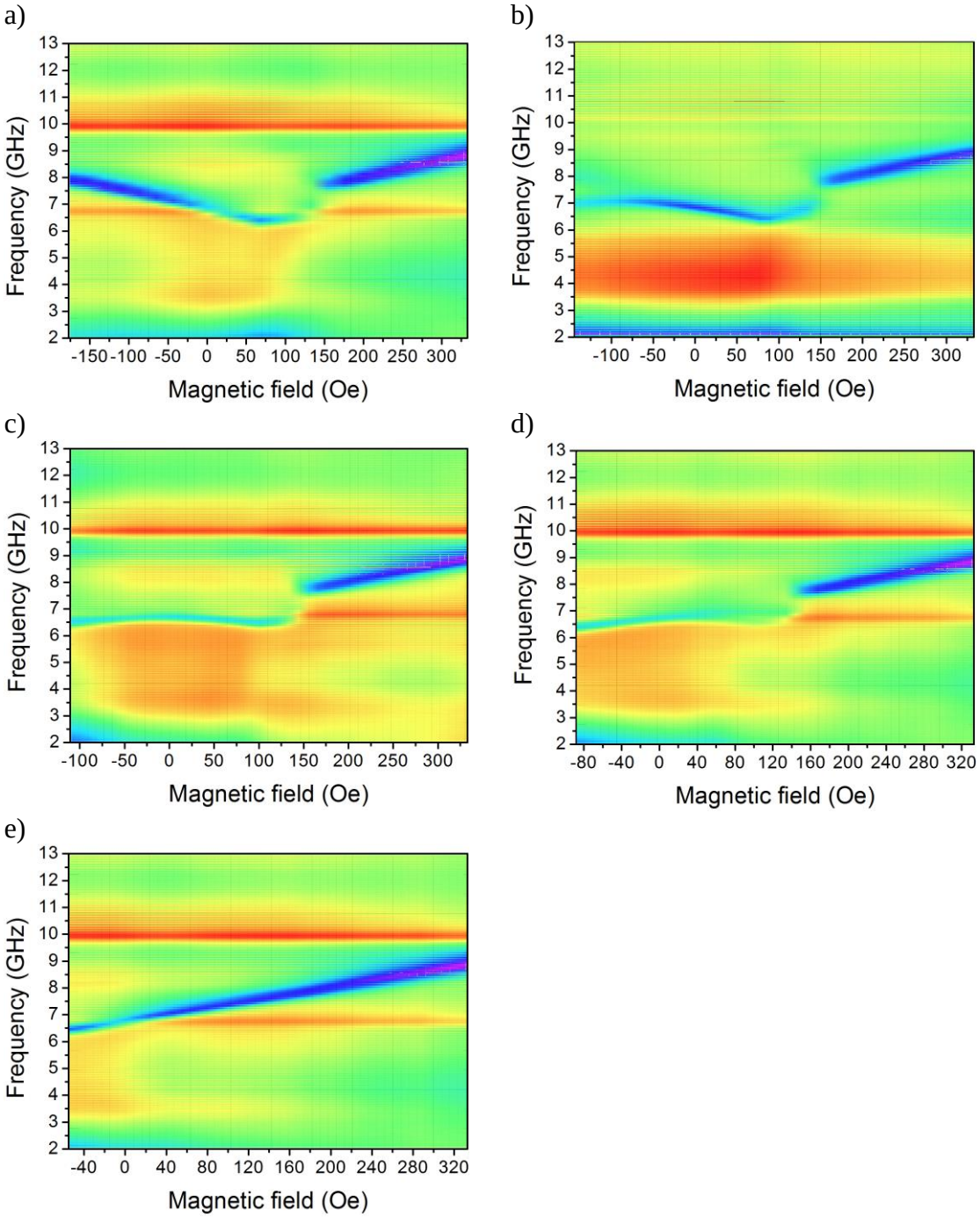

Figure 5.8 FMR absorption spectra in the minor loops with H_{min} = -177 Oe (a), -144 Oe (b), -111 Oe (c), -88 Oe (d) and -55 Oe (e) for periodic stripes array.

6. CONCLUSION

In this thesis preparation of the periodic and quasiperiodic $Ni_{80}Fe_{20}$ stripe magnonic structures using electron-beam lithography was optimized. During the process of their fabrication, only one layer of the PMMA 950K 1.5% resist was used to prevent stripes distortion. The resist thickness was measured for different rotational speed of substrates used during spin coating process and the suitable value was chosen. The proximity effect software correction was applied and the most adequate electron dose was selected. The process of the coplanar waveguides fabrication using direct laser writing was optimized in similar way as for the electron-beam lithography.

Static and dynamic magnetic properties of the fabricated stripes arrays were studied. Magneto optical Kerr effect was used to measure the hysteresis loops and image the magnetization reversal in the stripes. Because of insufficient setup resolution, not allowing observation of single stripes, magnetic force microscope was used. It allowed imaging the process of magnetization switching in the stripes in the field applied. Using coplanar waveguides integrated with the measured structures and vector network analyzer ferromagnetic resonance technique, spin excitations in these patterned films were studied. For the periodic structure one coercive field was found. Antiferromagnetic state was also observed in MFM images and excitation spectra. For quasiperiodic structure two coercive fields were observed, related to magnetization switch of wide and narrow stripes in respectively lower and higher fields. Not only the acoustic excitation mode was observed, but also additional one (optical mode) whose signal is related mostly to the narrow stripes.

BIBLIOGRAPHY

[1] J. Ding, M. Kostylev, and A. O. Adeyeye, "Magnetic hysteresis of dynamic response of one-dimensional magnonic crystals consisting of homogenous and alternating width nanowires observed with broadband ferromagnetic resonance," *Phys. Rev. B*, vol. 84, no. 5, Aug. 2011.

[2] V. V. Kruglyak, S. O. Demokritov, and D. Grundler, "Magnonics," *J. Phys. Appl. Phys.*, vol. 43, no. 26, p. 264001, 2010.

[3] M. Krawczyk and D. Grundler, "Review and prospects of magnonic crystals and devices with reprogrammable band structure," *J. Phys. Condens. Matter*, vol. 26, no. 12, p. 123202, Mar. 2014.

[4] H. Zhang, A. Hoffmann, R. Divan, and P. Wang, "Direct-current effects on magnetization reversal properties of submicron-size Permalloy patterns for radio-frequency devices," *Appl. Phys. Lett.*, vol. 95, no. 23, p. 232503, 2009.

[5] X. Zhu, D. A. Allwood, G. Xiong, R. P. Cowburn, and P. Grütter, "Spatially resolved observation of domain-wall propagation in a submicron ferromagnetic NOT-gate," *Appl. Phys. Lett.*, vol. 87, no. 6, p. 062503, 2005.

[6] A. V. Chumak, A. A. Serga, and B. Hillebrands, "Magnon transistor for all-magnon data processing," *Nat. Commun.*, vol. 5, p. 4700, Aug. 2014.

[7] S. Tacchi, M. Madami, G. Gubbiotti, G. Carlotti, S. Goolaup, A. O. Adeyeye, N. Singh, and M. P. Kostylev, "Analysis of collective spin-wave modes at different points within the hysteresis loop of a one-dimensional magnonic crystal comprising alternative-width nanostripes," *Phys. Rev. B*, vol. 82, no. 18, Nov. 2010.

[8] J. Ding, M. Kostylev, and A. O. Adeyeye, "Magnonic Crystal as a Medium with Tunable Disorder on a Periodical Lattice," *Phys. Rev. Lett.*, vol. 107, no. 4, Jul. 2011.

[9] J. Topp, D. Heitmann, M. P. Kostylev, and D. Grundler, "Making a Reconfigurable Artificial Crystal by Ordering Bistable Magnetic Nanowires," *Phys. Rev. Lett.*, vol. 104, no. 20, May 2010.

[10] C. Kittel, *Introduction to Solid State Physics*. New York: Wiley, 1966.

[11] R. W. Kelsall, I. W. Hamley, and M. Geoghegan, *Nanotechnologie*. Warszawa: Wydawnictwo Naukowe PWN, 2008.

[12] A. Aharoni, *Introduction to the Theory of Ferromagnetism*. New York: Oxford University Press, 1996.

[13] L. D. Landau and E. M. Lifshitz, "Theory of the dispersion of magnetic permeability in ferromagnetic bodies," *Phys. Z. Sowjetunion*, no. 8, pp. 153–169, 1935.

[14] T. L. Gilbert, "A Phenomenological Theory of Damping in Ferromagnetic Materials," *IEEE Trans. Magn.*, vol. 40, no. 6, pp. 3443–3449, Nov. 2004.

[15] T. Schwarze, "Spin Waves in 2D and 3D Magnonic Crystals: From Nanostructured Ferromagnetic Materials to Chiral Helimagnets," PhD Thesis, Technische Universiteaet Muenchen, Lehrstuhl für Physik funktionaler Schichtsysteme, E10, 2013.

[16] F. Giesen, "Magnetization dynamics of nanostructured ferromagnetic rings and rectangular elements," PhD Thesis, Universität Hamburg, Fachberbeich Physik, 2005.

[17] C. Kittel, "On the Theory of Ferromagnetic Resonance Absorption," *Phys Rev*, vol. 73, no. 155, 1948.

[18] C. Bilzer, “Microwave susceptibility of thin ferromagnetic films: metrology and insight into magnetization dynamics,” PhD Thesis, Université Paris-sud 11, Faculté des sciences d’Orsay, 2007.
[19] D. Stancil and A. Prabhakar, *Spin Waves Theory and Applications*. Boston, MA: Springer US, 2009.
[20] A. A. Serga, A. V. Chumak, and B. Hillebrands, “YIG magnonics,” *J. Phys. Appl. Phys.*, vol. 43, no. 26, p. 264002, Jul. 2010.
[21] S.-F. Hu, K.-D. Huang, Y.-M. Wan, and C.-L. Sung, “Proximity effect of electron beam lithography on single-electron transistors,” *Pramana*, vol. 67, no. 1, pp. 57–65, 2006.
[22] S. O. Demokritov, B. Hillebrands, and A. N. Slavin, “Brillouin light scattering studies of confined spin waves: linear and nonlinear confinement,” *Phys. Rep.*, vol. 348, no. 6, pp. 441–489, 2001.
[23] P. Kuświk, “Wpływ bombardowania jonowego na właściwości magnetyczne układów warstwowych Ni 80Fe 20/Au/Co/Au,” PhD Thesis, Institute of Molecular Physics Polish Academy of Science, Poznań, 2010.
[24] Discussion with Prof. Dr Maciej Krawczyk from Adam Mickiewicz University in Poznań

LIST OF TABLES

LIST OF FIGURES